Three-dimensional cellularization in chytrid fungi uses distinct mechanisms from those driving one- and two-dimensional cytokinesis in animals and yeast

Edgar M. Medina[1], Mary W. Elting[2], Lillian Fritz-Laylin[3]

[1]Department of Biology, University of Massachusetts, Amherst, MA, 01003, United States

[2]Cluster for Quantitative and Computational Developmental Biology and the Department of Physics, North Carolina State University, Raleigh, NC, 27695, United States

[3]Howard Hughes Medical Institute and the Department of Biology, University of Massachusetts, Amherst, MA, 01003, United States

ABSTRACT

Chytrid fungi provide a model for studying three-dimensional cellularization, where nuclei that are dispersed throughout the cytoplasm are synchronously compartmentalized into daughter cells. This organization poses geometric challenges not faced by cells undergoing conventional cytokinesis or *Drosophila* cellularization, where nuclei are organized in one- or two-dimensional arrangements. We use the chytrid *Spizellomyces punctatus* to show that chytrid cellularization begins with nuclei and centrosomes migrating to the plasma membrane, where centrosome-associated vesicles define sites of membrane invagination. The resulting tubular furrows extend, creating a foam-like tessellation of polyhedral compartments, each with a nucleus and cilium. Using inhibitors and laser ablation, we show that actomyosin networks drive cellularization, while microtubules pattern but are not essential for cellularization. Finally, we suggest that chytrids may have incorporated mechanisms associated with ciliogenesis in animals to coordinate the association of internal nuclei with actomyosin networks and membranes to solve the unique challenges associated with three-dimensional cellularization.

INTRODUCTION

Animal and fungal cells divide by forming a trench-like membrane furrow that separates daughter nuclei into two distinct compartments (Glotzer, 2017; Pollard and O'Shaughnessy, 2019). This type of cytokinesis usually occurs immediately after nuclear division with the two daughter nuclei arranged in a straight line. However, when multiple rounds of nuclear division occur before cytokinesis, the resulting multinuclear cell state must be resolved by more complex cellularization processes. During *Drosophila* development, for example, hundreds of nuclei arrange themselves in a uniform monolayer near the plasma membrane, making the outcome of cellularization a two-dimensional sheet of cells at the surface of the embryo (Sokac et al., 2023). Chytrid fungi represent an even more complex example that takes the geometry of cellularization to the third dimension. These deeply diverging lineages of fungi reproduce by compartmentalizing dozens of nuclei that are distributed homogeneously throughout the cytoplasm, resulting in a ball—or morula—of uninucleated daughter cells of uniform volume,

each bearing a motile cilium. The mechanisms that organize and drive this three-dimensional form of cellularization remain unclear.

Despite their different geometries, one-dimensional and two-dimensional cellularization involve the same four fundamental steps. First, nuclei find their positions. Second, the division site is selected. Third, the cell builds a cleavage structure at the division site. Fourth, the cleavage structure separates the mother cell into daughter cells. Animal and yeast cells use the same general strategies to complete these four steps. Both lineages rely on the pushing and pulling forces of microtubules to position their nuclei (Deshpande and Telley, 2021; Padilla et al., 2022; Xiang, 2018). Both use plasma membrane-anchored cues to define the position of the cleavage furrow (Glotzer, 2017; Pollard and O'Shaughnessy, 2019). Finally, both drive inward ingression of a trench-like furrow using a contractile ring made of actin and myosin-II (Glotzer, 2017; Pollard and O'Shaughnessy, 2019). Despite their widespread use across animals, yeasts, and slime molds, these basic strategies cannot be extrapolated directly to three-dimensional cellularization for two reasons. First, interior nuclei are obstructed from access to cues placed on the plasma membrane. Second, it is not obvious how the contraction of actomyosin rings assembled at the plasma membrane during one- and two-dimensional cellularization could generate the many planes needed to surround the inner nuclei present during three-dimensional cytokinesis. Thus, it remains unclear whether and how the mechanisms used for conventional cytokinesis and two-dimensional cellularization apply to three-dimensional chytrid cellularization.

Here, we dissect the molecular mechanisms driving three-dimensional cellularization in the chytrid fungus *Spizellomyces punctatus*. We identify the main stages of cellularization and use pharmacological and physical perturbations to disrupt them. We find that the molecular mechanisms driving chytrid cellularization involve a combination of actomyosin machinery similar to that used for conventional cytokinesis along with ciliogenesis-like events not seen in either conventional cytokinesis or *Drosophila* cellularization. One-, two-, and three-dimensional cellularization therefore together represent a key example of different cellular events that use overlapping molecular machinery for the same objective via distinct molecular mechanisms.

RESULTS

Membranes colocalize with actin and myosin-II to form a 3-dimensional cellularization lattice.

To begin, we confirmed that cellularization is indeed 3-dimensional in *Spizellomyces punctatus* (*Sp*). To determine the spatial distribution of nuclei and membrane during peak cellularization—the stage in which the network of cellularization furrows occupies the full cytoplasm of the mother cell—we developed a method to grow synchronized cultures of *Sp* adhered to glass imaging dishes (see methods). With this system, we tracked nuclei and membranes using a native nuclear localization signal fused to the fluorescent protein mClover3 and the fluorescent membrane dye FM4-64. Using 3D point-scanner confocal imaging, we found that during peak cellularization, each nucleus is enveloped inside a polyhedron-shaped membrane (**Figure 1A**). These uninucleated polyhedra are tightly packed throughout the spherical sporangium—like soap bubbles inside a container—confirming that chytrid cellularization is indeed three-dimensional.

To determine how the cellularization lattice forms, we conducted time-lapse microscopy of FM4-64-stained membranes during cellularization and identified five main stages of membrane

reorganization (**Figure 1B & C**). First, small, spherical invaginations form at the plasma membrane **(Stage 1)**. These "furrow initials" extend and elongate inwards toward the center of the cell, forming a membrane projection similar to a tubule, tunnel, or well that we call a "furrow" **(Stage 2)**. These furrows then invade the cytoplasm, branching and merging as they grow **(Stage 3)**, resulting in a tightly packed polyhedral network that occupies the entire sporangium **(Stage 4)**. Finally, in a single synchronous event of cell separation, called abscission, all of the polyhedra turn into individual spherical daughter cells **(Stage 5)**. The resulting individual cells then swim and/or crawl out of one or more discharge pores in the sporangial cell wall, leaving behind the empty shell of their mother .

To dissect in more detail the geometric patterning formed during chytrid cellularization, we measured the angles formed at the vertices of the cellularization polyhedra (**Figure 1D**) and the distribution of daughter zoospores generated via cellularization (**Figure 1E**). We found that in sporangial cross-sections, the cellularization lattice shows vertices with three furrows meeting on average at 120 degrees, consistent with zoospore territories of hexagonal symmetry. We also found that chytrid cellularization produces daughter zoospores of an average 2.89 micrometers in diameter, with 95% of cells within only 0.57 microns from this mean. This homogeneity represents only 60% more variation than artificial latex beads of 2 microns (**Figure 1E**). Together, these results show that the mechanisms of chytrid cellularization produce a tessellation of polyhedra of primarily hexagonal symmetry of very homogenous volume.

We next identified cellular machinery associated with the formation of the cellularization polyhedra. Animal and yeast cellularization relies on conserved cytoskeletal elements, primarily actin, myosin-II, and microtubules (Pollard and O'Shaughnessy, 2019). To explore the roles of these elements in chytrid cellularization, we visualized the distribution of actin networks with the actin polymer-binding probe Lifeact fused to the fluorescent protein mClover3 and co-stained cells with FM4-64. We found that during peak cellularization, both actin and membrane localize to the polyhedral cellularization lattice (**Figure 1F**). We next determined the distribution of a fluorescently-tagged myosin regulatory light chain (MRLC)—a proxy for myosin-II activity (Heissler and Sellers, 2015). We found that, like actin, the fluorescent MRLC colocalizes with the membrane in the cellularization lattice, suggesting a possible role of contractile actomyosin in chytrid cellularization (**Figure 1F**). Finally, by expressing a fluorescently tagged α-tubulin, we observed two structures closely associated with each nucleus during peak cellularization: a cilium as well as a centriolar microtubule organizing center and associated astral microtubules that extend from the centrosome toward the cell cortex (**Figure 1F**). Together, these results show that cellularization in chytrids may rely on similar cytoskeletal elements as those used by animal and yeast cells and that the assembly of the lattice is initiated at the plasma membrane, much like in yeast or animal cells. However, unlike animals and yeast, chytrids do not use typical trench-like furrows. Instead, chytrid furrows form as individual vesicles in the plasma membrane that extend into tubular "wells" that invade, merge, and weave together to form a tessellation of membrane polyhedra of homogenous volume and hexagonal symmetry.

Nuclear migration to the plasma membrane precedes the onset of cellularization.

In animal and yeast cytokinesis, as well as during *Drosophila* 2D cellularization, daughter nuclei remain stationary while cytokinetic furrows extend between or around them. Because nuclei remain highly dynamic during chytrid cellularization, it is unclear if nuclear position plays a role in defining the position, number, and assembly of furrows. To explore possible coordination between nuclear movement and furrow formation, we imaged synchronized cultures marked for

membranes with FM4-64 and for nuclei with a fluorescently tagged histone H2B. Imaging cross-sections through the center of sporangia revealed a possible enrichment of nuclei at the cell surface just before cellularization (**Figure 2A**). To quantify this observation, we calculated the ratio of nuclei in two regions of equivalent area: an outer donut at the surface of the sporangium and the remaining inner disk—the cortical nuclear ratio. This ratio was near one before and during cellularization, except for a short window of ten minutes during which nuclei are enriched in the cortical region (**Figure 2A-B**), a window that coincides with furrow initiation (Stage 1) and elongation (Stage 2). The maximal nuclear enrichment is closely associated with the start of furrow elongation (Stage 2), with 92% (22 out of 24) of sporangia progressing into furrow elongation (Stage 2) within five minutes of the peak nuclear cortical ratio (**Figure 2B; Supplementary Figure S1**). Thus, entry into cellularization is marked by the recruitment of nuclei to the plasma membrane.

To further explore the relationship between nuclear position and furrow initiation, we imaged at a higher frame rate and found that vesicular furrow initials form in proximity to the nuclei at the plasma membrane (**Figure 2C**). Imaging of the nuclei approaching entry into cellularization showed a progressive formation of vesicular furrow initials near cortical nuclei (**Figure 2C**). Because animal cells use astral microtubules to position furrows (Pollard and O'Shaughnessy, 2019), we hypothesized that patterning of chytrid cellularization may also involve microtubules. To test this hypothesis we followed cellularization in a strain expressing fluorescent tubulin (mClover3-alpha-Tubulin) in the presence of FM4-64 (**Figure 3A & B**). We found that each nucleus in an actively growing sporangium is associated with two opposing foci of tubulin fluorescence. Because these foci turn into spindle poles and duplicate immediately after nuclear division (**Supplementary Figure S2**), we infer that these foci represent centriolar centrosomes. Consistent with a role in furrow positioning for these microtubule organizing centers, we observed furrow initials forming in between the centrosomes and the plasma membrane (**Figure 3A & B**). To confirm that the furrows form near the centrosomes, we built a strain expressing a fluorescently tagged version of SAS-6, a core component of eukaryotic centrioles (Leidel et al., 2005). Cells expressing fluorescent SAS-6 show fluorescent foci at spindle poles and the base of the ciliary axoneme consistent with a centriolar distribution of SAS-6-mClover3. Upon entry into cellularization, SAS-6 puncta approach the plasma membrane, where they become associated with the furrow initials highlighted by FM4-64 (**Figure 3C**). These results show that during entry into cellularization, nuclei along with their associated centrosomes, are transiently recruited to the plasma membrane, where they mark the site—and may trigger the formation—of the vesicular furrow initials.

To further understand the relationship between furrow formation and nuclear positioning, we followed the position of nuclei, centrosomes, and membrane through the later stages of cellularization. Consistent with centrosomes playing a major role in organizing chytrid cellularization, we found that during furrow elongation (Stage 2) the centrosomes appear to remain tethered to the leading front of the furrow initials, dragging their nucleus with it. This behavior suggests that centrosomes may dock to the vesicular furrows, thereby tethering nuclei to the furrows during cellularization.

Microtubules are important for geometric patterning but are not necessary for cellularization.

Forces transmitted through microtubules help move and position nuclei and spindles during cytokinesis in animal and yeast systems (Burgess and Chang, 2005; Daga and Chang, 2005; Harvey, 1935; Rappaport, 1996, 1986). During *Drosophila* 2D cellularization, for example,

microtubules move and position the nuclei in a monolayer under the plasma membrane in preparation for cellularization (Baker et al., 1993; Deshpande et al., 2022; Sokac et al., 2023). Furthermore, plus end-directed motors that ride on microtubules (Kinesin-6; Pav-KLP) may provide the driving force required during the early stages of furrow ingression and deliver via vesicles the actin and membrane required during *Drosophila* 2D cellularization (Minestrini et al., 2003; Sokac et al., 2023; Sommi et al., 2010). We therefore wondered if the microtubules nucleated from chytrid centrosomes play a similar role in furrow elongation. To test this hypothesis, we treatedf cellularizing sporangia of a chytrid strain expressing fluorescent tubulin with 2μM Nocodazole. Unlike cells treated with the DMSO carrier alone, sporangia treated with Nocodazole showed rapid dissipation of all microtubule structures except for a bright dot at the centrosome (**Supplementary Figure S3**). Cells lacking microtubules formed cellularization polyhedra of uneven size with curved edges and rounded vertices **(Figure 4A)**. Despite these patterning defects, Nocodazole-treated sporangia completed cellularization and produced daughter cells that lacked cilia (**Supplementary Figure S3**). In contrast, sporangia treated with DMSO alone assembled well-organized cellularization lattices **(Figure 4A)** and produced normal, ciliated daughter cells.

To quantify the patterning defect induced by microtubule depolymerization, we compared the size and variance of the cellularization polyhedra between Nocodazole-treated and control cells. To aid automated image analysis, we focused on the polyhedra contiguous to the sporangial cell wall because they have regular, perpendicular furrows (**Figure 4A**). We found that, while sporangia treated with DMSO produced polyhedra with diameters between 3-3.5 microns, sporangia treated with Nocodazole produced polyhedra between 2.5-3 microns—a 14% reduction in diameter, with an even greater change in its variance (**Figure 4B**). These results show that, while microtubules are not strictly necessary for chytrid cellularization, they are key players in patterning cellularization.

The additional membrane needed for cellularization is sourced from the Golgi.

Building the three-dimensional cellularization lattice requires large amounts of membrane. Since the membrane used for cytokinesis in animals and yeasts comes from the Golgi, we wondered if this was also the case for chytrid cellularization. To test this hypothesis, we disrupted ER-to-Golgi trafficking with the drug Brefeldin A (BFA) (**Figure 4C, D, & E**). We treated synchronous populations of *Sp* with either 50 μM BFA—or DMSO carrier control—in the presence of FM4-64 and followed sporangial development by time-lapse imaging for six hours (**Figure 4C & D)**. To facilitate visualization of the cellularization pattern, we “unwrappedped” the circular sporangia by polar transformation (**Figure 3 C)**. While control sporangia completed cellularization within the imaging time window (N=127), only 7% of sporangia treated with BFA completed cellularization during the same period of time (N=206), 12 out of 14 of which had already started cellularization when BFA was added **(Figure 3 E)**. The sporangia that failed to cellularize displayed two main phenotypes. The first was “failure to start”. Sporangia with this phenotype were in either Stage 1 (pre-cellularization) or Stage 2 (with some level of furrow branching) upon BFA treatment **(Figure 3 D)**. Although the furrows of these cells made repeated movements toward the cell interior, these sporangia never progressed further in cellularization and eventually arrested cytoplasmic movement, vesiculated, and acquired intense, uniform FM4-64 fluorescence—suggestive of cell death. The second phenotype was “network collapse”, which occurred in sporangia that already had an advanced cellularization network (Stage 3) prior to BFA treatment (**Figure 3D**). The cellularization structures in these cells collapsed into a single disorganized bundle thatgradually disappeared followed by a death similar to that seen in “failure to start” phenotype. Together, these results show that ER-to-Golgi

trafficking is necessary for the formation and maintenance of the chytrid cellularization network and suggests that the membrane for cellularization is sourced primarily from the Golgi.

Actomyosin contraction is a driving force of chytrid 3D cellularization.

Having shown that microtubules are not necessary for chytrid cellularization, we next asked whether cellularization requires dynamic actin structures. We began by treating cellularizing sporangia expressing a fluorescently-tagged F-actin probe (Lifeact) with Latrunculin B (LatB)—a reversible inhibitor of actin polymerization that sequesters actin monomers preventing their incorporation into actin filaments and accelerates depolymerization (Coué et al., 1987; Fujiwara et al., 2018). Treatment with LatB caused a complete disassembly of the actin cellularization networks within five minutes (**Figure 5 A**). This effect was reversible, as the cellularization networks began reforming within five minutes of LatB wash out. We quantified these phenotypes using fluorescence intensity variability (*i.e.* Haralick image texture) as a proxy for the structural complexity of the actin networks (**Figure 5B**). While sporangia treated with DMSO alone showed no significant change in texture, sporangia treated with LatB showed a 50-75% increase in homogeneity within five minutes of treatment. Washout of LatB returned texture levels to pre-LatB levels within five minutes. Because Latrunculin B inhibits new F-actin assembly, these results indicate that cellularization networks require active actin polymerization.

In animals and yeast, similar-looking actin networks collaborate with myosin-II motors to generate the contractile forces that drive cytokinesis. To test if myosin-II is also necessary for chytrid cellularization, we treated cellularizing sporangia expressing Lifeact with the myosin-II inhibitor para-amino-blebbistatin (blebbistatin). While sporangia treated with the carrier control DMSO underwent normal cellularization, sporangia treated with blebbistatin failed to complete cellularization (**Figure 5C & D**). These results show that both actin polymerization and myosin-II activity are required for chytrid cellularization.

The actin networks that drive cellularization in animals and yeast rely on myosin-II activity to generate tension. The contractile properties of these networks can be tested using pulsed lasers to ablate actomyosin structures in a diffraction-limited spot and observe their movements (Kassianidou et al., 2017; Kumar et al., 2006; Moshtohry et al., 2022; Silva et al., 2016; Spira et al., 2017; Wollrab et al., 2016). If chytrid cellularization is powered by a similar contractile mechanism, then severing the actin furrows should cause remaining structures to recoil as they release tension (Moshtohry et al., 2022; Silva et al., 2016; Spira et al., 2017; Wollrab et al., 2016). We therefore used laser ablation to test if the actin networks of both early cellularization furrows and late cellularization polyhedra are under tension.

We first ablated furrows assembled during early cellularization (Stage 3), which caused large recoils of the actin structures (**Figure 6A**). Following the initial recoil, we observed a tendency of the ablated structures to contract back into the ablated area (**Figure 6A** kymographs). This "repair" response is consistent with the response to ablation in other contractile actin networks (Moshtohry et al., 2022; Silva et al., 2016; Spira et al., 2017; Wollrab et al., 2016). To quantify the speed and direction of the recoil, we turned to particle image velocimetry (PIV) (**Figure 6B-D**). By using the pixels from the actin network images as tracer particles, we could account for the variability in response across cellularization structures in different sporangia. This analysis shows that, after laser ablation, many of the F-actin structures within a few microns of the damaged region move with high velocities away from the ablation site (**Figure 6B**), indicating that neighboring contractile structures likely distribute their load onto each other.

To characterize the time scale and spatial extent of the response to ablation, we further analyzed the radial component of the PIV motion, either away from (recoil) or toward (repair) the site of ablation at different distances from the targeted region (**see Materials and Methods; Figure 6C, inset**). Consistent with the qualitative observations above, this analysis demonstrates an initial recoil response—indicated by a positive radial component of the velocity lasting around nine seconds—followed by a short period of movement towards the ablation site—indicated by a negative radial component of the velocity (**Figure 6C**, **Supplementary Figure 4**). While we see some variation in timing and magnitude among different sporangia, this overall signal is robust to different strategies of pre-processing and sampling of the data (**see Materials and Methods; Supplementary Figure 4-6**). We found the fastest recoil signal occurred between two and four microns from the ablation site(**Figure 6C, Supplementary Figure 5**) and between three and six seconds after ablation (**Figure 6D, Supplementary Figure 6**). Due to the comparable timescales of recoil, ablation itself (~1-2 seconds), and our imaging frequency (1 Hz) , there is significant uncertainty in the instantaneous magnitude of the recoil velocity, which may be faster than the ~75 nm/s we can detect (**Figure 6C and D**). However, the consistent recoil we observe for several frames following ablation shows that the actomyosin structures of early cellularization are indeed contractile, are under tension, and distribute their load over a distance of several microns.

Finally, we tested whether the F-actin polyhedra of late cellularization are also under tension. We observe a response that is similar in character as in early cellularization, but with faster recoil, suggesting higher tension by this stage. We found that laser ablation of the edges of the cellularization polyhedra resulted in a rapid recoil of the furrow tips away from the ablation site (**Figure 6E**), showing a displacement of approximately two microns within the first second after ablation followed by a shallow exponential recoil profile in which tension appear to release for more than 30 seconds (**Figure 6F**). After the first recoil, the two vertices at each side of the ablated furrow also recoiled away from each other, causing a dilation in adjacent polyhedra. Together, these results show that contractile actomyosin structures are used during furrow elongation as well as throughout the assembly of the cellularization polyhedra. Furthermore, F-actin network tension is important for establishing and maintaining the geometry of the cellularization network.

DISCUSSION

Here, we dissect the process of chytrid 3D cellularization into molecularly distinct stages (**Figure 7**). Cellularization onset is marked by the migration of nuclei and their associated, outward-facing centrosomes to the plasma membrane, followed by vesicle formation at the point where the centrosome abuts the plasma membrane. These membrane structures then project inward in an actomyosin-dependent process, turning into tubular “furrows” that drag the membrane and its attached nuclei into the cytoplasm. The furrows expand, branch, and merge using membrane sourced from the Golgi eventually settling into a tessellation of tightly-packed polyhedra of homogenous volume, each containing a single nucleus. Finally, the polyhedra synchronously separate from each other to form daughter cells that crawl or swim away through a hole in the cell wall of the mother. During cellularization, a centriole associated with each nucleus transitions into a basal body and grows a cilium. We show that, although chytrid cellularization requires actomyosin networks, it uses them in ways that are drastically different from those of animals and yeast.

Chytrids use actomyosin for cellularization but with different mechanisms from animal and yeast cytokinesis.

Chytrids use actomyosin in unique ways to drive three-dimensional cellularization, a process distinct from the actomyosin-driven one-dimensional cellularization conventional cytokinesis and from two-dimensional cellularization in *Drosophila*. Those one- and two-dimensional processes rely on the assembly of an actin ring at the plasma membrane that constricts and deforms the membrane into a trench-like furrow around each nucleus. Similarly, chytrids use actomyosin networks to drive membrane invagination during 3D cellularization. However, chytrid cellularization requires building furrows in regions of the cell that do not have ready access to the plasma membrane. Instead of building a furrow around each of the internal nuclei, chytrids recruit nuclei to the plasma membrane prior to furrow initiation and tether each nucleus to a furrow, maintaining their connection to the plasma membrane while the nuclei are moved inward. Then, tubular furrows are used to build the cellularization tessellation. This strategy neatly solves a problem not faced by animal or yeast model systems whose cellularization mechanisms have been well described.

Actomyosin-based multinuclear cellularization is not limited to chytrid fungi and *Drosophila*. The Ichtyosporeans *Sphaeroforma arctica* and *Creolimax fragrantissima* are unicellular relatives of animals that, like *Drosophila*, undergo two-dimensional multinuclear cellularization (Dudin et al., 2019; Suga and Ruiz-Trillo, 2013). The plasmodium of the acellular slime mold *Physarum polycephalum* also likely uses actomyosin for multinuclear cellularization (Goodman and Rusch, 1970; Okamura et al., 1983). Moreover, based on transitions from multinucleate to uninucleate cell states, multinuclear cellularization may also occur during the development and/or germination of slime mold sporocarps, structures that were likely present in the ancestor of the Amoebozoa (Kang et al., 2017). Because the shared ancestor of animals, fungi, and slime molds likely had a multinucleated stage (Skejo et al., 2021), it may have had the capacity to generate uninucleated propagules or gametes through multinuclear cellularization. Here we show that, like animals and Ichtyosporeans, chytrid fungi rely on actomyosin networks to drive multinuclear cellularization, suggesting that using actomyosin for this function may also be an ancestral feature of animals and fungi.

Chytrid cellularization combines ciliogenesis and cytokinetic mechanisms in a single cellularization program.

We have shown that chytrids solve the problem of surrounding non-peripheral nuclei with cleavage membranes by moving internal nuclei to the plasma membrane before redistributing them to the cytoplasm. This mechanism comprises three steps: recruitment of the centriole-nuclei to the membrane, the formation of vesicular furrows near each nuclear centrosome, and the tethering of the nuclei to these furrows via the centrosome. These activities resemble key stages of animal ciliogenesis. Ciliogenesis in animal cells starts with the migration of the centriole to the plasma membrane. During this migration, the distal end of one centriole recruits membrane to form a double-membrane sheet called the “ciliary vesicle”. This centriole then docks onto this ciliary vesicle to become a basal body and eventually fuses to the plasma membrane via the ciliary vesicle and assembles a ciliary axoneme that emerges from the cell (Zhao et al., 2023).

The morphological similarities between chytrid cellularization and animal ciliogenesis are remarkable. Chytrid vesicular furrow initials resemble animal ciliary vesicles in their vesicular appearance, in how they are formed near cortically migrating centrioles, and in how centrioles

appear to dock into them. Ultrastructural studies of chytrid ciliogenesis show a similar "vesicular"-like structure at internal basal bodies called a "primary flagellar vesicle" similar to the animal "ciliary vesicle" (Barron and Hill, 1974; Lessie and Lovett, 1968; Lowry and Roberson, 1997; Renaud and Swift, 1964). Upon recruitment to the plasma membrane, chytrid nuclei interact with the vesicular furrow initials via the centrosomal region. This attachment persists throughout the rest of cellularization, indicating that this form of nuclear tethering may be equivalent to centriolar docking in animal ciliogenesis that relies on genes associated with human ciliopathies (Tanos et al., 2013). Although many of these genes are also present in chytrids, we do not yet know if and how they are used during cellularization and/or ciliogenesis.

The molecular-level similarities between animal intracellular ciliogenesis and early chytrid cellularization are also remarkable. We found that Nocodazole treatment did not inhibit cellularization but did inhibit axonemal elongation. This is similar to ciliogenesis in the quail oviduct, where Nocodazole treatment did not inhibit centrosome migration or centriolar docking but did inhibit axoneme elongation (Boisvieux-Ulrich et al., 1989, 1987). Similarly, actin network perturbation disrupts both chytrid cellularization and centriolar migration in the quail oviduct (Boisvieux-Ulrich et al., 1990). Thus, chytrids may use animal-like ciliogenetic mechanisms to recruit the centrosomes and their nuclei to the plasma membrane. Because mechanistic details of centrosomal migration during animal ciliogenesis remain unclear (Hannaford and Rusan, 2024), the mechanisms of cortical nuclear migration in chytrids may shed light on centrosomal migration in animal ciliogenesis.

Using chytrids to explore the physics and geometry of foams in biological systems.

We have shown that chytrids cellularize by building a tessellation of polyhedra. We found that, although mother cells vary in size and number of nuclei, the daughter zoospores they produce are remarkably uniform in size. Daughter cell size is directly linked to the geometry of the polyhedra in the tesselation; polyhedra of homogenous volume give rise to daughters of homogenous volume. So how is the pattern, size, and symmetry of the tessellation of polyhedra generated? A hint may come from the similarity of chytrid cellularization to a system of packed soap bubbles, or "foam". A foam is a collection of surfaces that meet according to Joseph Plateau's Laws (1873) which state that thin soap films organize in a geometry that minimizes surface area for a given volume (Delsaulx, 1884; Plateau, 1873). More than 100 years ago, the mathematician and natural philosopher D'Arcy Thompson suggested that cellular partitions, tissues, and multicellular aggregates tend to follow the geometrical configurations of soap bubbles to minimize surface area (Thompson, 1945). Since then, the soap bubble analogy has been invoked to explain foam-like patterns in biological systems that arise through distinct mechanisms, such as extracellular force transmission across tissues, differential adhesion between cells, or space-constrained cell division (Agarwal and Zaidel-Bar, 2019; Hayashi and Carthew, 2004; Heer and Martin, 2017; Lecuit and Lenne, 2007). These processes start from separate individual bubbles that interact to eventually give rise to the foam. Although chytrid cellularization resembles these types of foams, the tesselations in this system do not begin with the formation of individual, separate bubbles. Instead, chytrids go straight to building a polyhedral foam wherein all interfacing surfaces and individual polyhedra are built *de novo*.

Generating zoospores is energetically expensive, and evolution may have selected for the most efficient way to compartmentalize a chytrid sporangium into zoospores of defined volume. Under this model, chytrids have evolved to solve a special case of Plateau's problem called *Kelvin's Problem*—finding the most efficient "tessellation of space into cells of equal volume

with the least surface area" (Thompson, 1887). Kelvin's problem must be solved by all biological systems that involve complete cellularization within a constrained volume. Therefore, understanding the mechanisms used by chytrids to solve Kelvin's problem can shed light on the principles of cellular morphogenesis across eukaryotic lineages, as well as inspire new strategies for solving geometrical problems within or without biological systems (Lecuit and Lenne, 2007).

Applying the soap bubble analogy to chytrid cellularization can also help us think about how chytrid mothers produce homogenous daughter cells. Plateau's laws state that: 1) the "bubbles" in the system should have smooth, unbroken surfaces, 2) all points on the same soap film surface have a constant mean curvature, 3) when soap bubble surfaces meet in threes they do so at an angle of 120 degrees—resulting in hexagonal symmetry—and 4) when they meet in fours they do so at an angle of 109.47—tetrahedral symmetry. Our observation of continuous and smooth cleavage membranes that, when meeting in three, form angles on average of hexagonal symmetry, and our ablation experiments that shows that neighboring furrows are mechanically connected, suggest that chytrid cellularization likely obeys at least the first three of these laws. If we assume that chytrid cellularization follows Plateau's Laws, then chytrids cellularize under three spatial constraints: the mother's cell volume is fixed, all compartments have the same "target" volume, and each compartment must contain a single nucleus. This raises important questions regarding the molecular mechanisms underlying how the target cell volume is defined and how the mother builds a compartment around each nucleus. Our results show that microtubule depolymerization results in patterning defects during chytrid cellularization similar to disruptions in nuclear spacing upon microtubule disruption in the distantly related zoosporic fungus *Allomyces* (Lowry and Roberson, 1997). Thus microtubules may help define proper nuclear spacing and a "minimal zoospore territory"—or "target volume"—during chytrid cellularization. Additionally, the tethering of nuclei to the cellularization furrows may help the mother cell keep track of all of the nuclei and serve as guides around which to build each polyhedron.

Concluding remarks.

Chytrid cellularization solves three-dimensional problems that neither animal nor yeast model systems face. Accordingly, we have found that chytrids fulfill each of the four fundamental steps of cellularization using mechanisms that consistently deviate from the general strategies deployed by animal and yeast model systems. First, in animal and yeast cytokinesis, nuclei find and hold their position while cleavage furrows move around them while chytrid nuclei are highly dynamic throughout cellularization. Second, animal and yeast systems rely on plasma membrane-associated cues to recruit and assemble the cytokinetic machinery. While conceptually simple for 1D and 2D cellularization, this constraint is problematic for 3D cellularization because most nuclei lie deep in the cytoplasm, surrounded by other nuclei, and are therefore spatially separated from plasma-membrane bound cues. We found that chytrids solve this problem by recruiting and attaching the nuclei to the plasma membrane, and *then* using actomyosin to build cleavage structures away from the plasma membrane. Third, while animal and yeast cells use trench-like furrows comprising membranes and actomyosin networks as cleavage structures, chytrids use tubular furrows of membranes and actomyosin that only later assemble into a polyhedron around each nucleus. How the tubular structures of early cellularization become polyhedra and how these polyhedra separate into daughter cells remain open questions. Finally, we found that chytrid cellularization may have co-opted ciliogenesis programs, raising the question of whether the similarity between these forms of cell division reflects analogy or homology at the molecular level. Taken together, we have found

that chytrids use conserved actomyosin machinery for three-dimensional cellularization but with different mechanisms from those of one- and two-dimensional cellularization—a clear reminder that conservation of machinery does not always signify conservation of mechanism.

ACKNOWLEDGEMENTS

The authors wish to thank Iain Patten for valuable conversations, advice, and feedback and the NCSU Cellular and Molecular Imaging Facility. This work was funded by NIH grant 1R35GM138083 to M.W.E. and NIH grant 1R35GM143039 to L.K.F.-L. who is Canadian Institute for Advanced Research (CIFAR) fellow in the Fungal Kingdom: Threats and Opportunities program and an Investigator of the Howard Hughes Medical Institute. EMM is a Howard Hughes Medical Institute Hanna H. Gray Fellow.

MATERIALS AND METHODS

Reporter construct design, strain generation, and molecular cloning. Constructs expressing Lifeact-mClover3v(EM112C: *H2Apr-Lifeact-mClover3-H2Ater:H2Bpr-P2A-T2A-hph-SynTer8*), Myosin light regulatory chain (MLRC) (SPPG_07268) fused to mClover3 (pEM110: *H2Apr-MLRC-mClover3-FLAG-MLRCter:H2Bpr-P2A-T2A-hph-SynTer8*), *Batrachochytrium dendrobatidis* alpha-Tubulin BDEG_00078 fused to mClover3 under the promoter of *Spizellomyces* alpha-Tubulin (SPPG_05136) (EM102: *AlphaTUBpr-mClover3-BdenAlphaTUB-BdTUBter:H2Bpr-P2A-T2A-hph-SynTer8*), *Spizellomyces* centriolar component SAS6 (SPPG_03341) fused to mClover3 (EM120: H2Apr-SAS6-mClover3-SAS6ter:H2Bpr-P2A-T2A-hph-SynTer8) were synthesized by Twist Bioscience (South San Francisco, United States) and cloned by Twist directly into the binary *Agrobacterium* plasmid pCAMBIA1300 (Addgene: 44183). Plasmids were transformed into *Spizellomyces* and transformant strains were recovered as described previously (Medina et al., 2020; Prostak et al., 2023). *Synther8* is a short synthetic terminator (No 8) from (Curran et al., 2015). Nuclear-localized mClover3 (GI3EM48; *H2Bpr-RbNLS-mClover3-ScADH1ter:H2Apr-hph-ScADH1ter*) was generated using previously published pGI3EM22C (*H2Bpr-Lifeact-tdTomato-ScADH1ter:H2Apr-hph-ScADH1ter*) (Medina et al., 2020) with Lifeact-tdTomato replaced by mClover3 with an N-terminal nuclear localization signal from *Spizellomyces* Rb protein SPPG_07796. Nuclear dynamics from Figure 2 were done with a strain carrying H2B-tdTomato from plasmid pGI3EM20C as previously described (Medina et al., 2020). We sequence-verified all constructs by whole-plasmid sequencing (Plasmidsaurus Inc.). Complete plasmid sequences and plasmids have also been deposited at Addgene.

Preparation of semi-synchronized cultures for live cell imaging. Two days prior to the experiment, use DS solution to harvest zoospores from an active culture of *Spizellomyces punctatus* (Koch type isolate NG-3) Barr (ATCC 48900) growing in K1 plates (50mg/L Carbenicillin and tetracycline) with or without selection (200mg/L Hygromycin) as done previously (Medina et al., 2020) and filter zoospores through sterile 40-micron mesh filter (fisherbrand Cat. No. 22363547) followed by a sterile Whatman No1 syringe filter (~11 micron). Plate 1mL of 1/5-1/10 dilution in DS solution of the zoospores into new K1 plates (right out of the fridge), seal with parafilm, and incubate for ~20-24h at 28 Celsius until peak zoospore release—zoospores are ready for seeding the imaging plates.

To prepare the imagining plates, a cellvis 6-well glass bottom black plate with lid (P06-1.5H-N) is cleaned with a plasma cleaner for four minutes at maximum level (Harrick Plasma Expanded Plasma Cleaner 115V). Add promptly 1mL per well of 25ug/mL filter-sterilized 50% w/v polyethyleneimine (PEI) (sigma-Aldrich P3143-100ML) and incubate at room temperature for 10 min. After the 10 min, remove the PEI solution and rinse 10 times with 2mL of sterile DS solution, then add 2mL of sterile DS in preparation for inoculation. Do not let the treated surface dry out. Proceed to prepare the zoospore inoculum.

To seed the imaging plate, harvest and filter the zoospores from the semi-synchronous plate culture made the day before using the same approach as above. Quantify zoospore concentration with a hemocytometer by counting 10uL from a 30uL 1:10 zoospore dilution including 3uL of Lugol solution (Sigma-Aldrich; 62650-100ML-F) (killing zoospores and increasing contrast). Dilute the zoospores with sterile DS to achieve a working stock of 1x10^6 zoospores per mL. Add 1mL of 1x10^6 zoospores per mL of zoospore solution to each well and leave for 10 min without moving at room temperature. After 10 minutes, tilt and remove the excess zoospore solution and replace it with 2mL of pre-warmed 28C K1 liquid media (50mg/mL carbenicillin; Fisher AAJ6194906), place on top of a 28C pre-warmed aluminum heatblock (two small tube heatblocks taped together) and leave for 10 min. After 10 min, wash gently three times with 2mL of liquid K1 (50mg/mL carbenicillin), then fill with 3mL of liquid K1 (50mg/mL carbenicillin), seal the plate with parafilm and incubate inside a closed plastic container with a humidity chamber (empty pipette tip box with perforated tip rack filled with 50mL water). Incubate for ~18h, at which point they are ready to start cellularization.

Live cell microscopy and laser ablation. For live cell imaging, cells were imaged on a Nikon Ti2 microscope equipped with a Crest X-Light V2 L-FOV spinning disk (50 µm pinhole), a Prime95B sCMOS camera (Photometrics), and a Plan Apo λ 100x 1.45 NA oil objective, and an Okolab stage top chamber (H301-K-FRAME) with humidity control. The illumination setup was a Celesta Light Engine solid-state laser launch (Lumencor), Celesta VCGRnIR pentaband emitter 10-10857, and Celesta VCGRnIR penta-band dichroic 10-10858. mClover3 Emission filter ET535/70m (Chroma), FM4-64 and tdTomato emission filter ET610/75m emission. The microscope was controlled through NIS -Elements software (Nikon).

Data for figures 1A and F imaging plates were prepared as described above, but before imaging a small 1.5% low-melt agarose (Sigma, A9045) pad made in K1 media was placed on top of the cells before imaging. Images were acquired using a Leica Stellaris 8 STED mounted on a Leica DMI8-CS base and using an HC PL APO CS2 86x/1.20 water objective, and Power HyD spectral detector. Images were acquired with White Light Laser (WLL) at 0.85 power percentage, taken at 1.31X zoom, 16x line averaging, 1024x1024 resolution, and mClover target wavelengths of 509.62-586.36nm and FM4-64 target wavelengths of 624.50-771.73nm. For three-dimensional reconstruction in Figure 1A, images were acquired at 1024x1024x130 with voxel size of 0.0254340084638276 x 0.0254340084638276 x 0.14839496124031007µm and visualized in ChimeraX-1.61 (Goddard et al., 2018; Pettersen et al., 2021) with gaussian smoothing of nuclei and membrane (sdev 0.05).

For laser ablation of F-actin structures during cellularization (Figure 6), imaging plates of a strain expressing Lifeact-mClover3 were prepared as described for live cell imaging but with a small (2mL) pad of 10% gelatin (Fisher Scientific G7-500) made in K1 media placed on top of the center of the well just before imaging. Imaging was done in a Nikon Ti-E microscope equipped with an Andor Dragonfly spinning disk confocal fluorescence microscope equipped

610 with 100x NA 1.45 objective (Nikon) and a built-in 1.5x magnifier; 488 nm diode laser with
611 Borealis attachment (Andor); emission filter Chroma ET525/50m; and an EMCCD camera
612 (iXon3, Andor Technology). Fusion software (Andor) was used to control data acquisition.
613
614 Ablations were performed using a MicroPoint (Andor) system with galvo-controlled steering to
615 deliver 20-30 3ns pulses of 551 nm light at 16-20 Hz (Andor) mounted on the Dragonfly
616 microscope described above, as previously described (Moshtohry et al., 2022;
617 Zareiesfandabadi and Elting, 2022). Fusion software (Andor) was used to control acquisition
618 while IQ software (Andor) was used simultaneously to control laser ablation. At this pulse rate,
619 the ablation process lasts ~2 s. Chroma ET610LP mounted in the dichroic position of a Nikon
620 filter turret was used to deliver the ablation laser to the sample. Since this filter also reflects the
621 mEGFP emission, the camera frames collected during the ablation process are blank. The
622 behavior of the severed F-actin structures of cellularization was imaged before and immediately
623 following laser ablation by acquiring a single confocal plane in the 488-nm channel every
624 second for at least one minute. The mechanism of ablative photodecomposition remains
625 unclear but may be caused by either the propagation of a pressure wave and/or cavitation
626 bubble dynamics (Rau et al., 2006; Venugopalan et al., 2002). The size of the damage is
627 approximately the size of the diffraction spot of the lens <0.4 μm in the XY plane and <0.8 μm
628 in the Z axis (Khodjakov et al., 1997).
629
630 **Pharmacological perturbations during live-cell imaging.** About one hour before the start of
631 the experiment (~17h), remove excess of dislodged sporangia by removing gently 2mL of the
632 media and replacing it with 2mL of fresh prewarmed K1+Carb media, adding and removing
633 liquid from opposite sides of the well. Repeat this wash thrice in total. To the remaining 1mL,
634 add 1mL of 20uM FM4-64 (stock 1mg/mL in water) made in K1+Carb media for staining the
635 plasma membrane. Bring to the microscope and place in a preheated Okolab stage top
636 chamber (H301-K-FRAME) with humidity control (30 Celsius). Twenty individual sporangia
637 were selected from a single well for time-lapse imaging. Imaging started at 18h, sampling every
638 3 or 5 min, for six hours. Pharmacological perturbations are applied by removing 1mL of media
639 and replacing it with 2X working solution of the drug of choice. For washout experiments, 50%
640 of the final volume of the well is replaced with fresh pre-heated media ten times. Cells were
641 treated with 2uM final concentration of Nocodazole (Cayman Chemical; No. 13857) or
642 equivalent volume of DMSO, 50uM of Brefeldin A (Sigma B7651) or equivalent volume of
643 DMSO, 10uM Latrunculin B (Millipore, 428020) or equivalent volume of ethanol, 150uM
644 p-a-blebbistatin (Cayman 22699) or equivalent volume of DMSO.
645
646
647 **Coulter Counter cell size measurements.** 1mL of zoospores from six independent culture
648 plates of *Spizellomyces* were freshly harvested as described in the section on
649 semi-synchronized cultures for live imaging was placed in a 25mL Accuvette (A35473;
650 Beckman Coulter) with 24mL of freshly made 50% dilution of Isoton II diluent (C96980;
651 Beckman Coulter) and run through a 10uM aperture tube (B42812; Beckman Coulter) on a
652 Coulter Counter Multisizer 4e (B23005; Beckman Coulter) running on a freshly made 50%
653 dilution of Isoton II diluent (C96980; Beckman Coulter). The Coulter counter is calibrated with
654 2-micron latex beads (C72513 CC; Beckman Coulter). The size distribution of zoospores and
655 beads was exported as CSV, then processed, and visualized using JupyterLab 1.16 and R
656 v4.1.2 facilitated by custom scripts (Kluyver et al., 2016; R Core Team, 2013).
657
658
659 **Image processing and analyses.** To measure the angle distribution in the polyhedral
660 tessellation of cellularization (Figure 1D), five sporangia from three independent biological

661 replicates of control cells stained with FM4-64 and imaged during cellularization were selected.
662 The frame before obvious signs of cellularization was selected for each sporangium and the
663 angles between the three cleavage planes (tri-furrow) around at least ten different nodes
664 (where furrows meet) were measured using the angle function of Fiji (Schindelin et al., 2012).
665 As a positive control and a gauge of technical reproducibility, an artificially perfect 120-degree
666 tri-furrow with similar proportions of thickness-length was used for generating an artificial
667 dataset by transposition and measured the same way at the same time. The resulting dataset
668 was processed and visualized using JupyterLab 1.16 and R v4.1.2 facilitated by custom scripts
669 (Kluyver et al., 2016; R Core Team, 2013).
670
671 For measuring nuclear cortical migration dynamics (Figure 2A & B) we used scikit-image (Van
672 der Walt et al., 2014) image processing in Python with custom scripts in a Google Collab
673 notebook. Briefly, elliptical sporangia were masked, and segmented and an ellipse was fitted to
674 their perimeter. A second ellipse with 70% of radii from the perimeter ellipse was used as the
675 boundary between the outer and inner 50% of the sporangial area. The nuclei were segmented
676 via thresholding and watershed algorithms. The cortical nuclear ratio is the number of nuclei in
677 the outer donut relative to the inner disk for each frame in the time-lapse video. The resulting
678 measures were then processed and visualized using JupyterLab 1.16 and R v4.1.2 facilitated
679 by custom scripts (Kluyver et al., 2016; R Core Team, 2013).
680
681 To measure the defect in patterning observed after Nocodazole treatment in cellularizing
682 sporangia (Figure 4A & B), an ellipse was masked and fitted to circular sporangia as described
683 above using scikit-image (Van der Walt et al., 2014) image processing in Python with custom
684 scripts in a Google Collab notebook. Briefly, since the cleavage furrows of the outer layer of
685 daughter cells are perpendicular to the perimeter cell wall, and thus size estimates are likely to
686 be more accurate, a concentric ellipse at 0.85% of the fitted perimeter ellipse was drawn. The
687 peak-to-peak distance along the profile of the FM4-64 fluorescence intensity along the
688 perimeter of this ellipse was used as a proxy for daughter cell diameter. The resulting
689 measures were then processed and visualized using JupyterLab 1.16 and R v4.1.2 facilitated
690 by custom scripts (Kluyver et al., 2016; R Core Team, 2013). The statistical significance test
691 was a one-tailed permutation test of the difference of means.
692
693 The effects of Brefeldin A on cellularization were visualized by similar sporangial segmentation
694 and masking followed by log-polar transform using sci-kit-image (Van der Walt et al., 2014)
695 image processing in Python with custom scripts in a Google Collab notebook. The phenotyping
696 of the sporangia (success, Failure to Start, Network Collapse) was done by hand in Fiji
697 (Schindelin et al., 2012). The resulting measures were then processed and visualized using
698 JupyterLab 1.16 and R v4.1.2 facilitated by custom scripts (Kluyver et al., 2016; R Core Team,
699 2013).
700
701 To measure the effects of Latrunculin B on the F-actin structures during cellularization,
702 sporangia of circular shape that did not move excessively during the experiment were selected
703 and imported to CellProfiler 4.2.1 (McQuin et al., 2018) for segmentation. As a proxy of the
704 level of cellularization in the actin structures, we used Haralick measures of texture (Haralick et
705 al., 1973), the Angular Second Moment relative to the time-point right before LatB
706 treatment—relative homogeneity—was used for visualization. The phenotyping of the effects of
707 p-a-Blebbistatin on cellularization (completion or failure) was done by hand in Fiji (Schindelin et
708 al., 2012).
709
710 For Particle Image Velocimetry (PIV) analyses, selected sporangia were masked in Fiji
711 (Schindelin et al., 2012) and analyzed with OpenPIV-0.25.0 (Liberzon et al., 2021) through

custom Python scripts in a Google Collab Notebook. Vector field plots (Figure 6B) and plots from the top 10% velocity vectors per PIV timepoint (Figure 6C) were generated in JupyterLab 1.16 and R v4.1.2 facilitated by custom scripts (Kluyver et al., 2016; R Core Team, 2013). Kymographs from Figure 6A were generated using Fiji (Schindelin et al., 2012) from regions 20-pixel wide centered and parallel to the ablated furrow. Recoil displacement analyses from laser ablation of late-stage polyhedra were performed via sci-kit-image (Van der Walt et al., 2014) image processing in Python with custom scripts in a Google Collab notebook. Briefly, a 10-pixel wide region centered in a line along the ablated furrow was used to measure the mean fluorescence intensity profile along the furrow. Intensity peaks were detected and used to locate and measure the inter-peak distance between the receding tips of the ablated furrow. The results were visualized using JupyterLab 1.16 and R v4.1.2 facilitated by custom scripts (Kluyver et al., 2016; R Core Team, 2013).

A main concern during our analysis was the difference in time between image acquisition before and after ablation and the time required for ablation. PIV uses the displacement of tracer particles (pixels showing fluorescence of F-actin in our case) between consecutive images to estimate the changes in direction and velocity of the tracer particles. Although we imaged every second before and after laser ablation, it takes about two seconds to perform the 20-30 pulses of the laser required to sever the actin structures and one more second to remove filters and take the next image. Thus, our images before and after ablation are separated by three seconds, while in reality, there is about one second from the end of the laser ablation until the acquisition of the first image “post” ablation. Furthermore, we do not have the “real” image of the sporangium just before ablation, only before ablation is started. To navigate this problem we could assume that the sporangium before the start of ablation is a good proxy of the status of the actin structures before the end of ablation, and thus run our PIV analysis using a sampling time of one second before and after ablation. Alternatively, we can run the PIV analysis using three seconds as the sampling time between images, which would underestimate by up to three-fold the velocities in response to ablation, but it would be accurate about the true time difference between images. A second concern is that when all pixels within sporangium are used as tracer particles, we would detect displacement not only in cleavage structures but also movements of the fluorescent probe in the cytoplasm.

We tested different strategies of resampling and filtering the ablation data of a sporangium to assess their effects on the recoil signal retrieved by PIV (**Supplementary Figure 4**). We performed basic thresholding (MultiOtsu) to remove the cytoplasmatic signal, resampled the complete time-series every three seconds to reflect the true time difference between pre-ablation and post-ablation images, combined thresholding and resampling, and combined resampling with a mask (generated from the sum of all frames before ablation followed by MultiOtsu thresholding) to restrict the PIV to the cleavage structures. To measure the displacement caused by ablation, we retrieved vectors with magnitude greater than zero and that pass PIV signal to noise ratio test and calculated their radial component of the velocity (V) relative to the ablation site ($\mathcal{A}$) (**Figure 6C cartoon**). This measure ($V_{\mathcal{A}}$) represents, for a velocity vector anywhere in the sporangium, the part of the velocity vector that is in the direction of the ablation site $\mathcal{A}$. This allows us to probe specifically the displacement velocities away ($V_{\mathcal{A}}>0$) or towards ($V_{\mathcal{A}}<0$) the ablation site irrespective of the complexity of geometry and movement of the actin structures across the sporangium. We found that the recoil signal is robust to different strategies of data processing, thus we decided to use three-second resampling of the dataset without thresholding as the main data processing for our analyses and discussion.

Quantification of recoil displacement after ablation of the structures of late cellularization (**Figure 6E-F**) performed by calculating the distance between severed furrow tips. Tip position defined as the peak in the fluorescence intensity distribution in a line 10-pixel wide along the ablated cleavage plane (white dotted rectangle in inset).

REFERENCES

Agarwal, P., Zaidel-Bar, R., 2019. Principles of Actomyosin Regulation In Vivo. Trends Cell Biol. 29, 150–163. https://doi.org/10.1016/j.tcb.2018.09.006

Baker, J., Theurkauf, W., Schubiger, G., 1993. Dynamic changes in microtubule configuration correlate with nuclear migration in the preblastoderm *Drosophila* embryo. J. Cell Biol. 122, 113–121. https://doi.org/10.1083/jcb.122.1.113

Barron, J.L., Hill, E.P., 1974. Ultrastructure of Zoosporogenesis in *Allomyces macrogynus*. J. Gen. Microbiol. 80, 319–327. https://doi.org/10.1099/00221287-80-2-319

Boisvieux-Ulrich, E., Lainé, M.C., Sandoz, D., 1990. Cytochalasin D inhibits basal body migration and ciliary elongation in quail oviduct epithelium. Cell Tissue Res. 259, 443–454. https://doi.org/10.1007/BF01740770

Boisvieux-Ulrich, E., Lainé, M.C., Sandoz, D., 1989. *In vitro* effects of colchicine and nocodazole on ciliogenesis in quail oviduct. Biol. Cell 67, 67–79. https://doi.org/10.1111/j.1768-322x.1989.tb03011.x

Boisvieux-Ulrich, E., Laine, M.C., Sandoz, D., 1987. I *n vitro* effects of benzodiazepines on ciliogenesis in the quail oviduct. Cell Motil. Cytoskeleton 8, 333–344. https://doi.org/10.1002/cm.970080406

Burgess, D.R., Chang, F., 2005. Site selection for the cleavage furrow at cytokinesis. Trends Cell Biol. 15, 156–162. https://doi.org/10.1016/j.tcb.2005.01.006

Coué, M., Brenner, S.L., Spector, I., Korn, E.D., 1987. Inhibition of actin polymerization by latrunculin A. FEBS Lett. 213, 316–318. https://doi.org/10.1016/0014-5793(87)81513-2

Curran, K.A., Morse, N.J., Markham, K.A., Wagman, A.M., Gupta, A., Alper, H.S., 2015. Short Synthetic Terminators for Improved Heterologous Gene Expression in Yeast. ACS Synth. Biol. 4, 824–832. https://doi.org/10.1021/sb5003357

Daga, R.R., Chang, F., 2005. Dynamic positioning of the fission yeast cell division plane. Proc. Natl. Acad. Sci. U. S. A. 102, 8228–8232. https://doi.org/10.1073/pnas.0409021102

Delsaulx, J., 1884. Les travaux scientifiques de Joseph Plateau. A. Vromant.

Deshpande, O., de-Carvalho, J., Vieira, D.V., Telley, I.A., 2022. Astral microtubule cross-linking safeguards uniform nuclear distribution in the *Drosophila* syncytium. J. Cell Biol. 221, e202007209. https://doi.org/10.1083/jcb.202007209

Deshpande, O., Telley, I.A., 2021. Nuclear positioning during development: Pushing, pulling and flowing. Semin. Cell Dev. Biol. 120, 10–21.

https://doi.org/10.1016/j.semcdb.2021.09.020

Dudin, O., Ondracka, A., Grau-Bové, X., Haraldsen, A.A., Toyoda, A., Suga, H., Bråte, J., Ruiz-Trillo, I., 2019. A unicellular relative of animals generates a layer of polarized cells by actomyosin-dependent cellularization. eLife 8, e49801. https://doi.org/10.7554/eLife.49801

Fujiwara, I., Zweifel, M.E., Courtemanche, N., Pollard, T.D., 2018. Latrunculin A Accelerates Actin Filament Depolymerization in Addition to Sequestering Actin Monomers. Curr. Biol. CB 28, 3183-3192.e2. https://doi.org/10.1016/j.cub.2018.07.082

Glotzer, M., 2017. Cytokinesis in Metazoa and Fungi. Cold Spring Harb. Perspect. Biol. 9, a022343. https://doi.org/10.1101/cshperspect.a022343

Goddard, T.D., Huang, C.C., Meng, E.C., Pettersen, E.F., Couch, G.S., Morris, J.H., Ferrin, T.E., 2018. UCSF ChimeraX: Meeting modern challenges in visualization and analysis. Protein Sci. Publ. Protein Soc. 27, 14–25. https://doi.org/10.1002/pro.3235

Goodman, E.M., Rusch, H.P., 1970. Ultrastructural changes during spherule formation in *Physarum polycephalum*. J. Ultrastruct. Res. 30, 172–183. https://doi.org/10.1016/s0022-5320(70)90071-7

Hannaford, M.R., Rusan, N.M., 2024. Positioning centrioles and centrosomes. J. Cell Biol. 223, e202311140. https://doi.org/10.1083/jcb.202311140

Haralick, R.M., Shanmugam, K., Dinstein, I.H., 1973. Textural features for image classification. IEEE Trans. Syst. Man Cybern. 610–621.

Harvey, E.B., 1935. The mitotic figure and cleavage plane in the egg of *Parechinus microtuberculatus*, as influenced by centrifugal force. Biol. Bull. 69, 287–297.

Hayashi, T., Carthew, R.W., 2004. Surface mechanics mediate pattern formation in the developing retina. Nature 431, 647–652. https://doi.org/10.1038/nature02952

Heer, N.C., Martin, A.C., 2017. Tension, contraction and tissue morphogenesis. Development 144, 4249–4260. https://doi.org/10.1242/dev.151282

Heissler, S.M., Sellers, J.R., 2015. Four things to know about myosin light chains as reporters for non-muscle myosin-2 dynamics in live cells. Cytoskelet. Hoboken NJ 72, 65–70. https://doi.org/10.1002/cm.21212

Kang, S., Tice, A.K., Spiegel, F.W., Silberman, J.D., Pánek, T., Cepicka, I., Kostka, M., Kosakyan, A., Alcântara, D.M.C., Roger, A.J., Shadwick, L.L., Smirnov, A., Kudryavtsev, A., Lahr, D.J.G., Brown, M.W., 2017. Between a Pod and a Hard Test: The Deep Evolution of Amoebae. Mol. Biol. Evol. 34, 2258–2270. https://doi.org/10.1093/molbev/msx162

Kassianidou, E., Brand, C.A., Schwarz, U.S., Kumar, S., 2017. Geometry and network connectivity govern the mechanics of stress fibers. Proc. Natl. Acad. Sci. U. S. A. 114, 2622–2627. https://doi.org/10.1073/pnas.1606649114

Khodjakov, A., Cole, R.W., Rieder, C.L., 1997. A synergy of technologies: combining laser microsurgery with green fluorescent protein tagging. Cell Motil. Cytoskeleton 38, 311–317. https://doi.org/10.1002/(SICI)1097-0169(1997)38:4<311::AID-CM1>3.0.CO;2-6

Kluyver, T., Ragan-Kelley, B., Pérez, F., Granger, B., Bussonnier, M., Frederic, J., Kelley, K., Hamrick, J., Grout, J., Corlay, S., 2016. Jupyter Notebooks–a publishing format for reproducible computational workflows, in: Positioning and Power in Academic Publishing: Players, Agents and Agendas. IOS press, pp. 87–90.

Kumar, S., Maxwell, I.Z., Heisterkamp, A., Polte, T.R., Lele, T.P., Salanga, M., Mazur, E., Ingber, D.E., 2006. Viscoelastic retraction of single living stress fibers and its impact on cell shape, cytoskeletal organization, and extracellular matrix mechanics. Biophys. J. 90, 3762–3773. https://doi.org/10.1529/biophysj.105.071506

Lecuit, T., Lenne, P.-F., 2007. Cell surface mechanics and the control of cell shape, tissue patterns and morphogenesis. Nat. Rev. Mol. Cell Biol. 8, 633–644. https://doi.org/10.1038/nrm2222

Leidel, S., Delattre, M., Cerutti, L., Baumer, K., Gönczy, P., 2005. SAS-6 defines a protein family required for centrosome duplication in *C. elegans* and in human cells. Nat. Cell Biol. 7, 115–125. https://doi.org/10.1038/ncb1220

Lessie, P.E., Lovett, J.S., 1968. Ultrastructural changes during sporangium formation and zoospore differentiation in *Blastocladiella emersonii*. Am. J. Bot. 55, 220–236.

Liberzon, A., Käufer, T., Bauer, A., Vennemann, P., Zimmer, E., 2021. OpenPIV/openpiv-python: OpenPIV-Python v0.23.4. https://doi.org/10.5281/zenodo.4409178

Lowry, D.S., Roberson, R.W., 1997. Microtubule organization during zoosporogenesis in *Allomyces macrogynus*. Protoplasma 196, 45–54. https://doi.org/10.1007/BF01281057

McQuin, C., Goodman, A., Chernyshev, V., Kamentsky, L., Cimini, B.A., Karhohs, K.W., Doan, M., Ding, L., Rafelski, S.M., Thirstrup, D., 2018. CellProfiler 3.0: Next-generation image processing for biology. PLoS Biol. 16, e2005970.

Medina, E.M., Robinson, K.A., Bellingham-Johnstun, K., Ianiri, G., Laplante, C., Fritz-Laylin, L.K., Buchler, N.E., 2020. Genetic transformation of *Spizellomyces punctatus*, a resource for studying chytrid biology and evolutionary cell biology. eLife 9, e52741. https://doi.org/10.7554/eLife.52741

Minestrini, G., Harley, A.S., Glover, D.M., 2003. Localization of Pavarotti-KLP in living *Drosophila* embryos suggests roles in reorganizing the cortical cytoskeleton during the mitotic cycle. Mol. Biol. Cell 14, 4028–4038. https://doi.org/10.1091/mbc.e03-04-0214

Moshtohry, M., Bellingham-Johnstun, K., Elting, M.W., Laplante, C., 2022. Laser ablation reveals the impact of Cdc15p on the stiffness of the contractile ring. Mol. Biol. Cell 33, br9. https://doi.org/10.1091/mbc.E21-10-0515

Okamura, S., Hayashi, K., Nishi, A., 1983. Participation of actin filaments in the plasmodial

915 cleavage of spherulating *Physarum polycephalum*. J. Gen. Appl. Microbiol. 29, 73–77.
916 https://doi.org/10.2323/jgam.29.73
917
918 Padilla, J.R., Ferreira, L.M., Folker, E.S., 2022. Nuclear movement in multinucleated cells. Dev.
919 Camb. Engl. 149, dev200749. https://doi.org/10.1242/dev.200749
920
921 Pettersen, E.F., Goddard, T.D., Huang, C.C., Meng, E.C., Couch, G.S., Croll, T.I., Morris, J.H.,
922 Ferrin, T.E., 2021. UCSF ChimeraX: Structure visualization for researchers, educators,
923 and developers. Protein Sci. Publ. Protein Soc. 30, 70–82.
924 https://doi.org/10.1002/pro.3943
925
926 Plateau, J.A.F., 1873. Statique expérimentale et théorique des liquides soumis aux seules
927 forces moléculaires: Tome premier. Gauthier-Villars.
928
929 Pollard, T.D., O'Shaughnessy, B., 2019. Molecular Mechanism of Cytokinesis. Annu. Rev.
930 Biochem. 88, 661–689. https://doi.org/10.1146/annurev-biochem-062917-012530
931
932 Prostak, S.M., Medina, E.M., Kalinka, E., Fritz-Laylin, L.K., 2023. A guide to
933 *Agrobacterium*-mediated transformation of the chytrid fungus *Spizellomyces punctatus*.
934 Access Microbiol. 5, acmi000566.v3. https://doi.org/10.1099/acmi.0.000566.v3
935
936 R Core Team, 2013. R: A language and environment for statistical computing. Found. Stat.
937 Comput. Vienna Austria.
938
939 Rappaport, R., 1996. Cytokinesis in animal cells. Cambridge University Press.
940
941 Rappaport, R., 1986. Establishment of the mechanism of cytokinesis in animal cells. Int. Rev.
942 Cytol. 105, 245–281. https://doi.org/10.1016/s0074-7696(08)61065-7
943
944 Rau, K.R., Quinto-Su, P.A., Hellman, A.N., Venugopalan, V., 2006. Pulsed laser
945 microbeam-induced cell lysis: time-resolved imaging and analysis of hydrodynamic
946 effects. Biophys. J. 91, 317–329. https://doi.org/10.1529/biophysj.105.079921
947
948 Renaud, F.L., Swift, H., 1964. The Development of Basal Bodies and Flagella in *Allomyces*
949 *arbusculus*. J. Cell Biol. 23, 339–354. https://doi.org/10.1083/jcb.23.2.339
950
951 Schindelin, J., Arganda-Carreras, I., Frise, E., Kaynig, V., Longair, M., Pietzsch, T., Preibisch,
952 S., Rueden, C., Saalfeld, S., Schmid, B., Tinevez, J.-Y., White, D.J., Hartenstein, V.,
953 Eliceiri, K., Tomancak, P., Cardona, A., 2012. Fiji: an open-source platform for
954 biological-image analysis. Nat. Methods 9, 676–682. https://doi.org/10.1038/nmeth.2019
955
956 Silva, A.M., Osório, D.S., Pereira, A.J., Maiato, H., Pinto, I.M., Rubinstein, B., Gassmann, R.,
957 Telley, I.A., Carvalho, A.X., 2016. Robust gap repair in the contractile ring ensures
958 timely completion of cytokinesis. J. Cell Biol. 215, 789–799.
959 https://doi.org/10.1083/jcb.201605080
960
961 Skejo, J., Garg, S.G., Gould, S.B., Hendriksen, M., Tria, F.D.K., Bremer, N., Franjević, D.,
962 Blackstone, N.W., Martin, W.F., 2021. Evidence for a Syncytial Origin of Eukaryotes
963 from Ancestral State Reconstruction. Genome Biol. Evol. 13, evab096.
964 https://doi.org/10.1093/gbe/evab096
965

Sokac, A.M., Biel, N., De Renzis, S., 2023. Membrane-actin interactions in morphogenesis: Lessons learned from *Drosophila* cellularization. Semin. Cell Dev. Biol. 133, 107–122. https://doi.org/10.1016/j.semcdb.2022.03.028

Sommi, P., Ananthakrishnan, R., Cheerambathur, D.K., Kwon, M., Morales-Mulia, S., Brust-Mascher, I., Mogilner, A., 2010. A mitotic kinesin-6, Pav-KLP, mediates interdependent cortical reorganization and spindle dynamics in *Drosophila* embryos. J. Cell Sci. 123, 1862–1872. https://doi.org/10.1242/jcs.064048

Spira, F., Cuylen-Haering, S., Mehta, S., Samwer, M., Reversat, A., Verma, A., Oldenbourg, R., Sixt, M., Gerlich, D.W., 2017. Cytokinesis in vertebrate cells initiates by contraction of an equatorial actomyosin network composed of randomly oriented filaments. eLife 6, e30867. https://doi.org/10.7554/eLife.30867

Suga, H., Ruiz-Trillo, I., 2013. Development of ichthyosporeans sheds light on the origin of metazoan multicellularity. Dev. Biol. 377, 284–292. https://doi.org/10.1016/j.ydbio.2013.01.009

Tanos, B.E., Yang, H.-J., Soni, R., Wang, W.-J., Macaluso, F.P., Asara, J.M., Tsou, M.-F.B., 2013. Centriole distal appendages promote membrane docking, leading to cilia initiation. Genes Dev. 27, 163–168. https://doi.org/10.1101/gad.207043.112

Thompson, D.W., 1992. On Growth and Form, 1st ed. Cambridge University Press. https://doi.org/10.1017/CBO9781107325852

Thompson, W., 1887. On the division of space with minimal partitional area. Philos. Mag. 24, 503.

Van der Walt, S., Schönberger, J.L., Nunez-Iglesias, J., Boulogne, F., Warner, J.D., Yager, N., Gouillart, E., Yu, T., 2014. scikit-image: image processing in Python. PeerJ 2, e453.

Venugopalan, V., Guerra, A., Nahen, K., Vogel, A., 2002. Role of laser-induced plasma formation in pulsed cellular microsurgery and micromanipulation. Phys. Rev. Lett. 88, 078103. https://doi.org/10.1103/PhysRevLett.88.078103

Wollrab, V., Thiagarajan, R., Wald, A., Kruse, K., Riveline, D., 2016. Still and rotating myosin clusters determine cytokinetic ring constriction. Nat. Commun. 7, 11860. https://doi.org/10.1038/ncomms11860

Xiang, X., 2018. Nuclear movement in fungi. Semin. Cell Dev. Biol. 82, 3–16. https://doi.org/10.1016/j.semcdb.2017.10.024

Zareiesfandabadi, P., Elting, M.W., 2022. Force by minus-end motors Dhc1 and Klp2 collapses the *S. pombe* spindle after laser ablation. Biophys. J. 121, 263–276. https://doi.org/10.1016/j.bpj.2021.12.019

Zhao, H., Khan, Z., Westlake, C.J., 2023. Ciliogenesis membrane dynamics and organization. Semin. Cell Dev. Biol. 133, 20–31. https://doi.org/10.1016/j.semcdb.2022.03.021

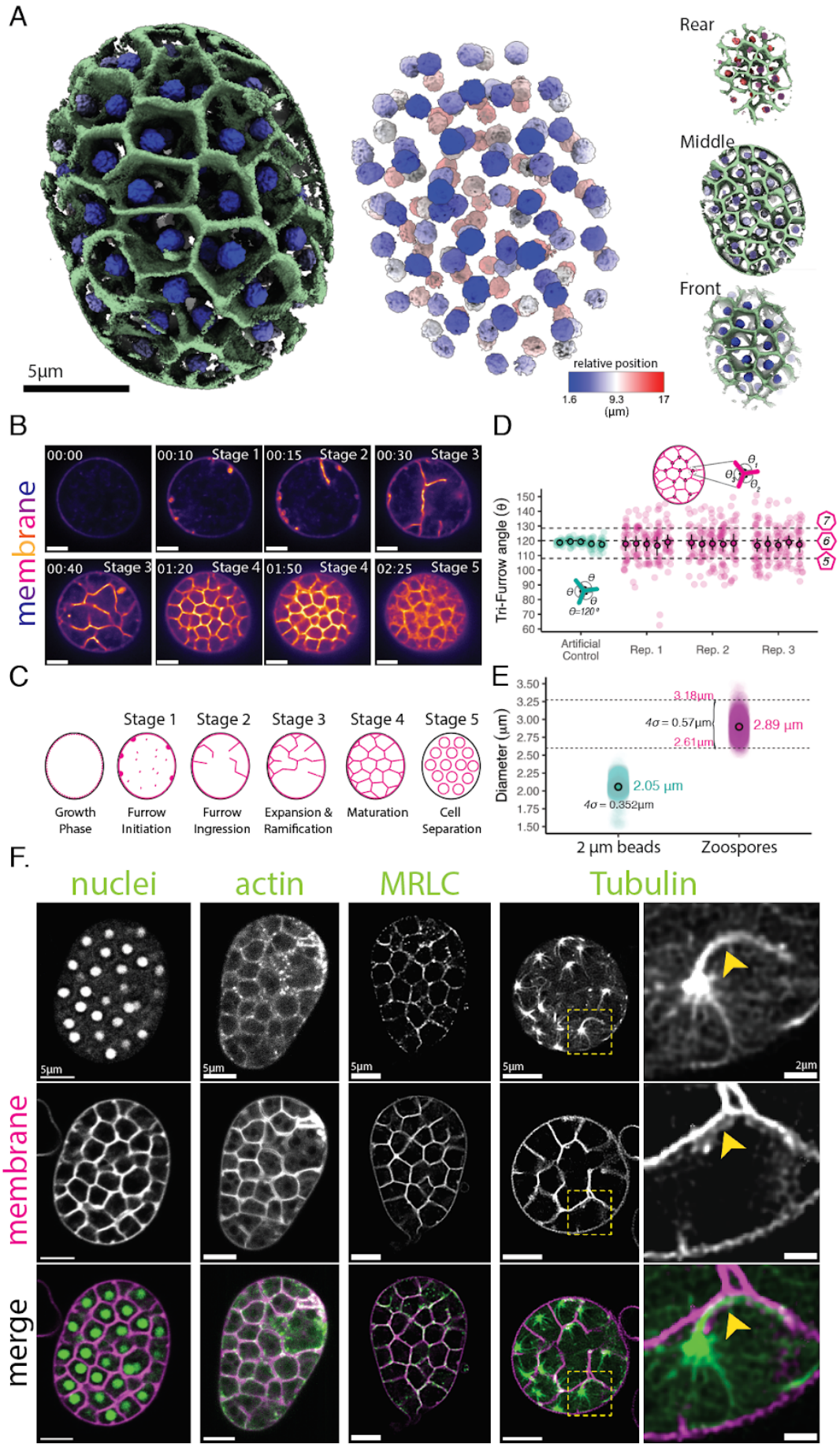
A
5µm
relative position
1.6
9.3
17
(µm)
Rear
Middle
Front
B
membrane
00:00
00:10
Stage 1
00:15
Stage 2
00:30
Stage 3
00:40
Stage 3
01:20
Stage 4
01:50
Stage 4
02:25
Stage 5
C
Stage 1
Stage 2
Stage 3
Stage 4
Stage 5
Growth Phase
Furrow Initiation
Furrow Ingression
Expansion & Ramification
Maturation
Cell Separation
D
Tri-Furrow angle (θ)
θ=120°
Artificial Control
Rep. 1
Rep. 2
Rep. 3
E
Diameter (µm)
3.18µm
4σ = 0.57µm
2.89 µm
2.61µm
2.05 µm
4σ = 0.352µm
2 µm beads
Zoospores
F.
nuclei
actin
MRLC
Tubulin
membrane
merge
5µm
2µm

1018 **Figure 1. The chytrid *Spizellomyces* cellularizes by building a 3D tessellation of**
1019 **membrane polyhedra of homogeneous size, hexagonal symmetry, and demarcated by**
1020 **actin and myosin-II activity. (A)** ChimeraX 3D reconstruction from a point scanner confocal
1021 live-cell image of a chytrid sporangium at peak cellularization. Membrane polyhedra are
1022 uninucleated and homogeneously distributed across the volume of the sporangium (front,
1023 middle, rear). FM-64 dye was used for membrane (green) and nuclear-localized mClover3 for
1024 highlighting nuclei (blue to red). The nuclear position is shown as relative depth from the first
1025 stack image. **(B & C)** Images and schematic of the five main stages of development of the
1026 membrane cleavage structures of chytrid cellularization. **(D)** The cellularization polyhedra have
1027 internal vertices with angles in agreement with hexagonal symmetry (magenta). The angles
1028 were measured for at least twenty vertices within the central slice of a sporangium and for five
1029 sporangia in three biological replicates. These angles were compared to a set of five artificial
1030 vertices (teal) with perfect hexagonal symmetry (120 degrees) and similar cleavage membrane
1031 thickness and proportions to assess technical measurement error. **(E)** Chytrid cellularization is
1032 very precise in the production of daughter cells of similar size. Distribution of sizes of artificial
1033 latex beads of 2µm (teal) compared to chytrid zoospores (magenta). 95% of zoospores are
1034 within 0.57µm of the mean (2.89µm). $N_{zoospores}$ = 3785, N_{beads}= 7272. Measurements made with
1035 a Coulter counter. **(F)** Actin and myosin-II colocalize with the membrane of the cellularization
1036 polyhedra. Live-cell confocal imaging of strains expressing the (nuclei) NLS-mClover3 to track
1037 nuclei (same image used in 3D reconstruction in A), the F-actin probe Lifeact-mClover3 (actin),
1038 the myosin-II probe MRLC-mClover3 (MRLC), and mClover3-α-Tubulin (Tubulin) to track
1039 microtubules. The magnified region of microtubules highlights the ciliary axoneme (yellow
1040 arrow) that starts elongating after entry into cellularization. Membrane dyed with FM4-64. Scale
1041 5µm.

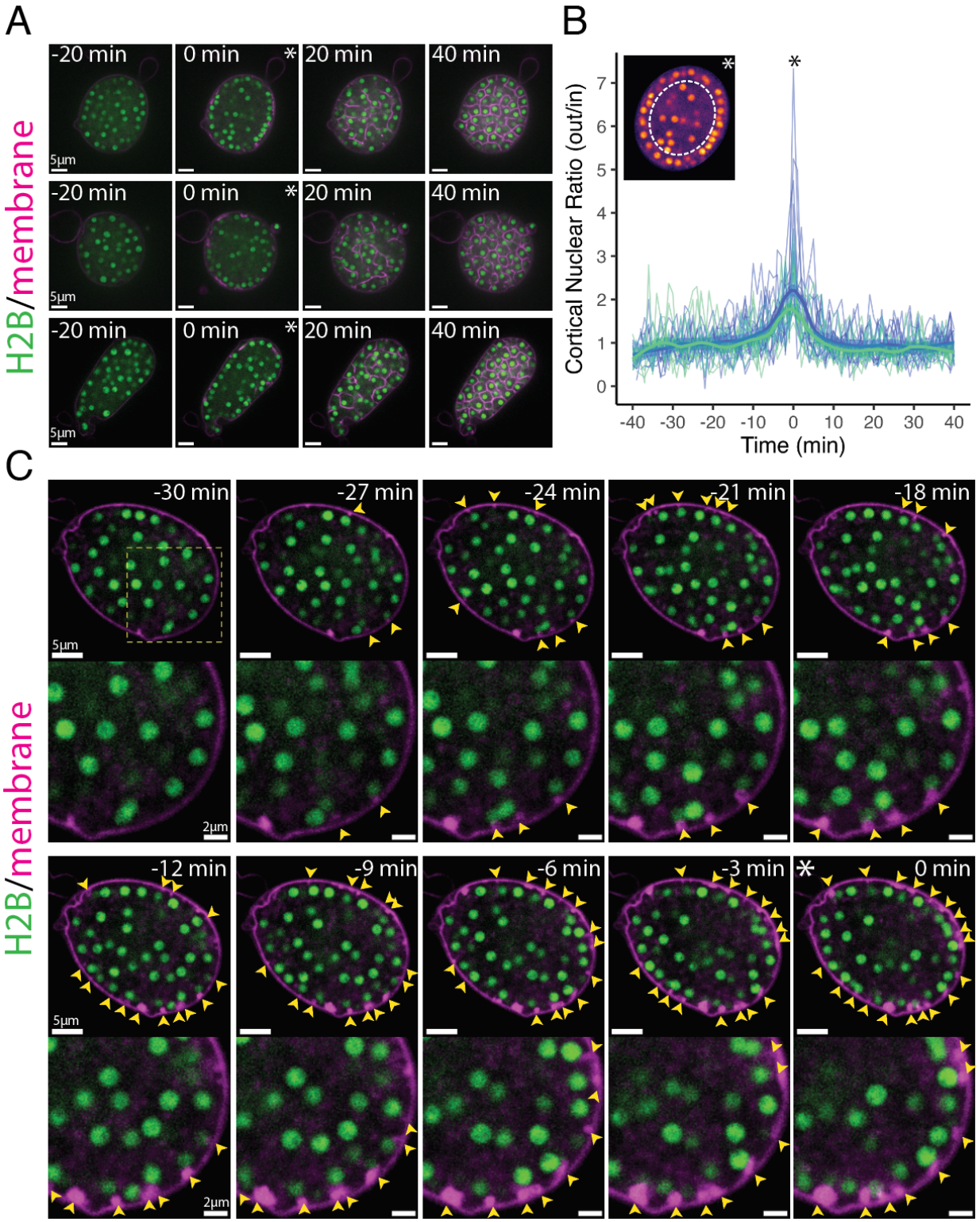

Figure 2. The onset of chytrid cellularization is marked by the recruitment of nuclei to the plasma membrane and the formation of vesicular membrane structures near cortical nuclei. (A) Chytrid nuclei (H2B-tdTomato) are homogeneously distributed across the

1047 sporangium before (-20 min) and after (+20 min) entry into cellularization except for a narrow
1048 window just at entry into cellularization (0 min; asterisk; coincides with the formation of the first
1049 membrane vesicles; Stage 1) when nuclei are enriched at the plasma membrane. **(B)** Nuclear
1050 enrichment at the plasma membrane is limited to a narrow window of time (~10 min) at the
1051 onset of cellularization. After, the nuclei return to be homogeneously distributed. Quantification
1052 of nuclear dynamics during time-lapse microscopy 40 min before and after entry into
1053 cellularization. The cortical nuclear ratio (CNR) corresponds to the ratio of the number of nuclei
1054 in the outer 50% area (a donut) relative to the inner 50% area (disk)—see inset image. The
1055 CNR distribution during time-lapse imaging for each sporangium was centered on zero based
1056 on the peak cortical nuclear ratio—marked with an asterisk. Blue and green signify two different
1057 biological replicates with thin lines showing individual sporangia and thick lines indicating loess
1058 regressions (99% confidence interval; span=0.2). **(C)** Recruitment of nuclei to the plasma
1059 membrane during entry into cellularization coincides with the formation of membrane vesicular
1060 structures (yellow arrows) in the proximity of each nucleus. Progression of nuclear recruitment
1061 and concomitant vesicular furrow initiation shown until peak cortical migration (asterisk; 0 min).

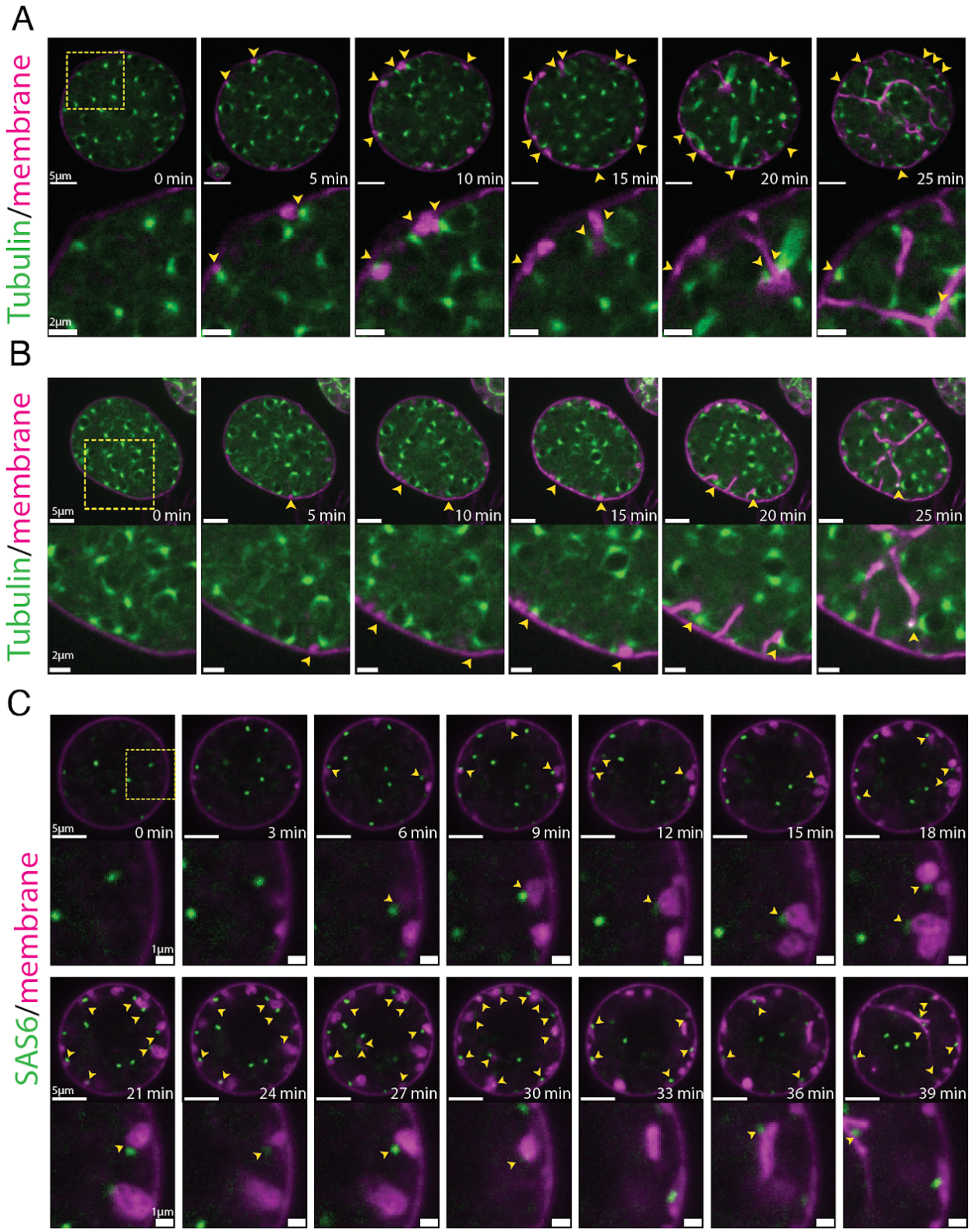
A
Tubulin/membrane
5µm
0 min
5 min
10 min
15 min
20 min
25 min
2µm
B
Tubulin/membrane
5µm
0 min
5 min
10 min
15 min
20 min
25 min
2µm
C
SAS6/membrane
5µm
0 min
3 min
6 min
9 min
12 min
15 min
18 min
1µm
5µm
21 min
24 min
27 min
30 min
33 min
36 min
39 min
1µm

Figure 3. Cortical nuclei attach to the membrane vesicular furrow initials via the centrosomal region and are then dragged inwards when the vesicular furrows are elongated. (A & B) membrane vesicular furrows form in the proximity of the nuclear centrosomal regions (yellow arrows; 5-to-15min). The nuclei remain tethered to the membrane via the centrosomal region when the vesicular furrows extend inwards (15-to-25 min). Note that in (A) a nucleus forms a spindle and remains attached via the polar region of the spindle to the extending furrow. **(C)** A strain expressing a fluorescently tagged centrosomal component SAS6-mClover3 shows that the centrioles are proximal to the vesicular furrow initials (yellow arrows) and remain attached to the furrows during elongation. Membrane dyed with FM4-64.

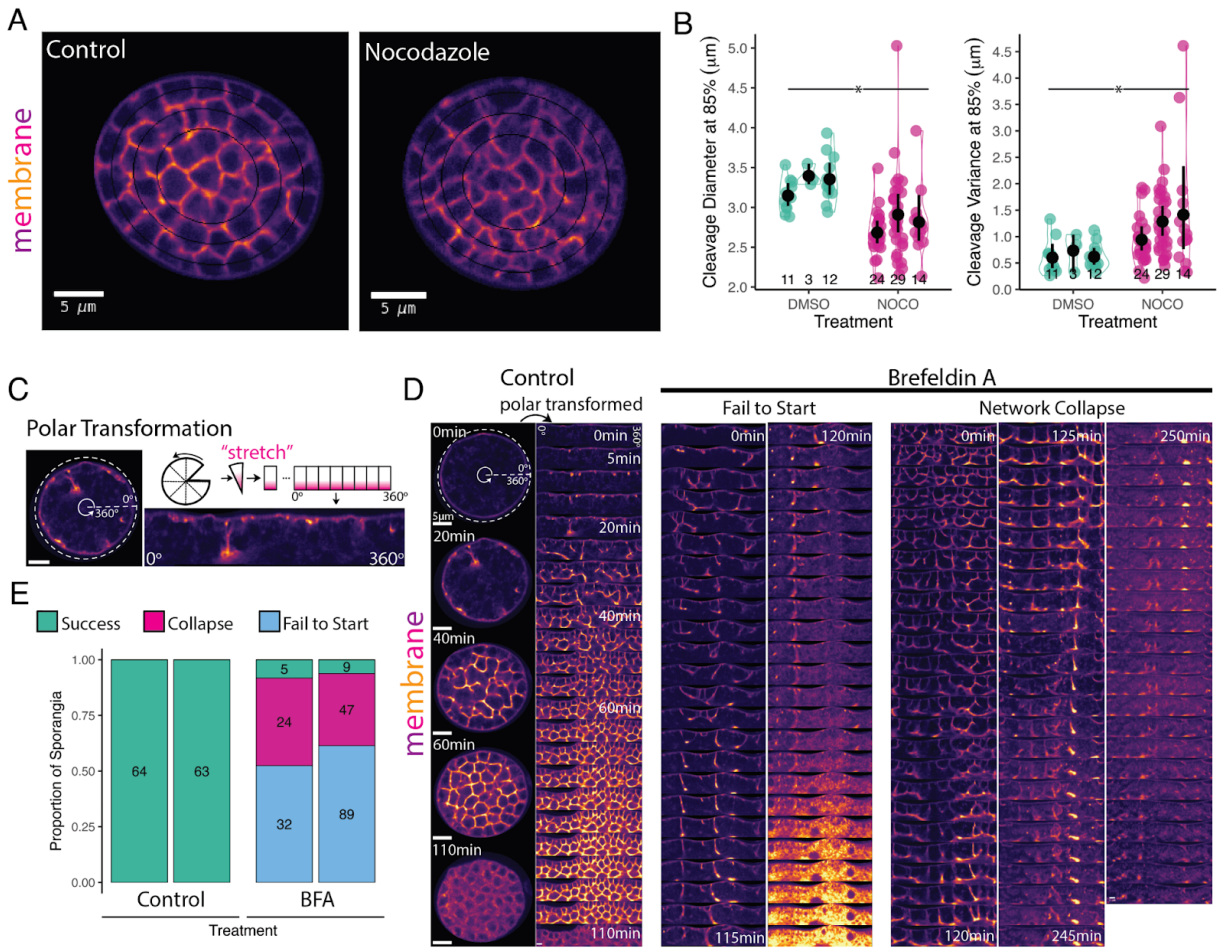

Figure 4. Depolymerization of microtubules does not inhibit cellularization but causes patterning defects and the membrane of cellularization is sourced primarily from the Golgi. (A) Sporangia treated with Nocodazole (2μM) during cellularization causes a defect in the geometric patterning of cellularization but does not inhibit it. Concentric ellipses of 85%, 65%, and 45% radii are shown in thin black lines **(B)** Daughter cells of sporangia treated with Nocodazole are smaller and are more variable in diameter than sporangia treated with the carrier control DMSO. The daughter size was estimated using the distance between max-intensity peaks in a line scan of the fluorescence intensity of the membrane along the 85% radii ellipse. Cleavage planes at 85% tend to be perpendicular to the ellipse and thus more accurate. Significance was assessed by a permutation test of the difference of means. * p-value ≤ 0.05. **(C)** Schematic of the polar transformation on an image of membrane organization (FM4-64) in a sporangium during cellularization. This transformation converts "circular" images with polar coordinates into "unwrapped" images in cartesian coordinates for easier visualization. In our case, the plasma membrane will be at the top and the furrows invade inwards towards the bottom. **(D)** Sporangia treated during cellularization with the inhibitor of ER-to-Golgi trafficking Brefeldin-A fail to complete cellularization because they either fail to start—furrows try to invade but fail to progress (left)—or cause collapse of the furrows already formed at the moment of treatment (right). In contrast, control sporangia treated with the carrier DMSO show a gradual increase in the complexity of patterning until completing cell separation (110 min). Bright FM4-64 fluorescence in the "fail to start" panel corresponds to cell death. **(E)** Quantification of the proportion of cells succeeding, failing to start, or collapsing during treatment with BFA or DMSO control.

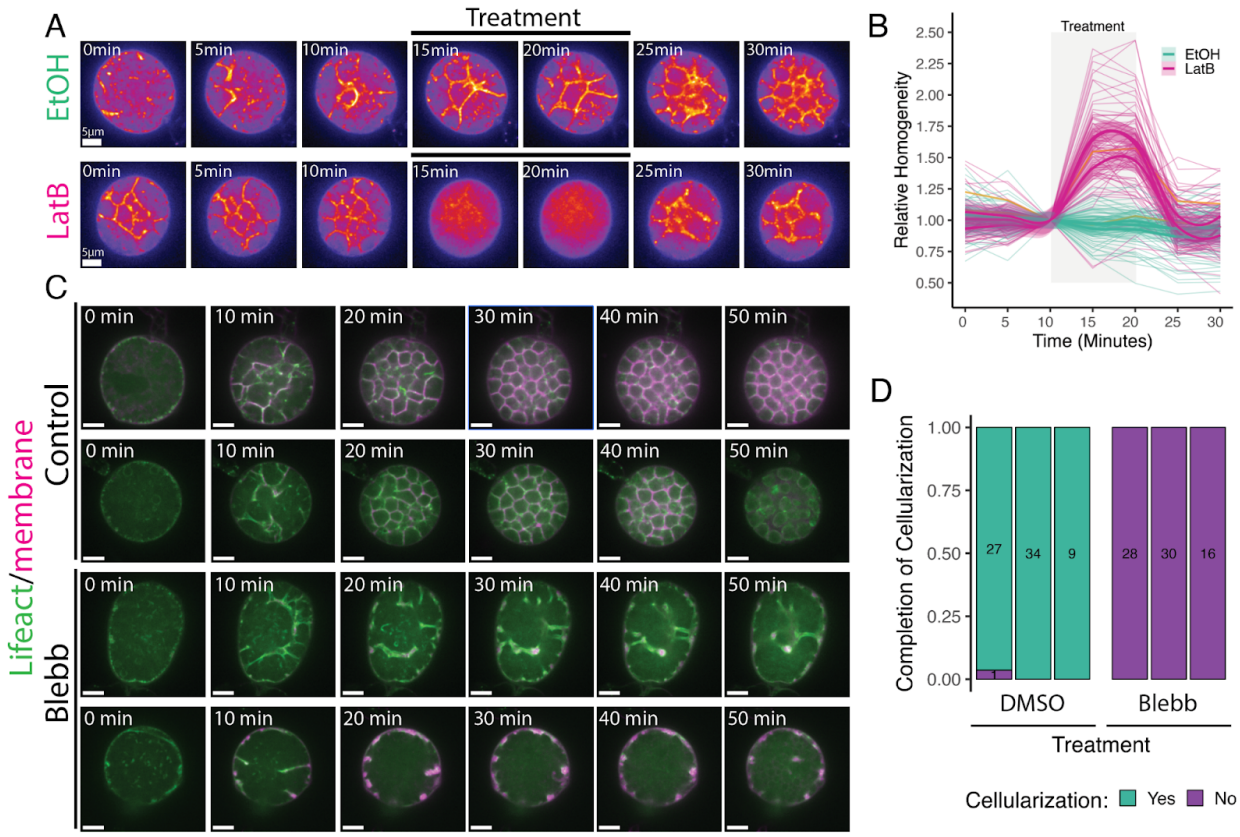

Figure 5. Chytrid cellularization requires actin polymerization and myosin-II activity. (A) Inhibition of actin polymerization with Latrunculin B (LatB) causes disassembly of the actin cellularization network. This network is reassembled within 5 min after the washout of LatB. **(B)** Treatment with LatB (magenta) causes a sharp increase in sporangial homogeneity—reduction in texture, and thus disassembly of the actin network—that comes back to pre-treatment levels after the washout of LatB. Control sporangia (teal) treated with DMSO control shows no effect. The mean line and bootstrapping 95% confidence interval of the mean are shown for three biological replicates. Orange lines show the series shown in panel (A). **(C)** Treatment of sporangia with the inhibitor of myosin-II activity para-amino-blebbistatin (Blebb) inhibits cellularization. Control cells treated with DMSO control show normal cellularization, while sporangia treated with Blebb fail to advance beyond Stage 1 or 2. **(D)** Treatment of sporangia with Blebb completely inhibits cellularization. The box for each of the three biological replicates shows the number of sporangia analyzed per replicate.

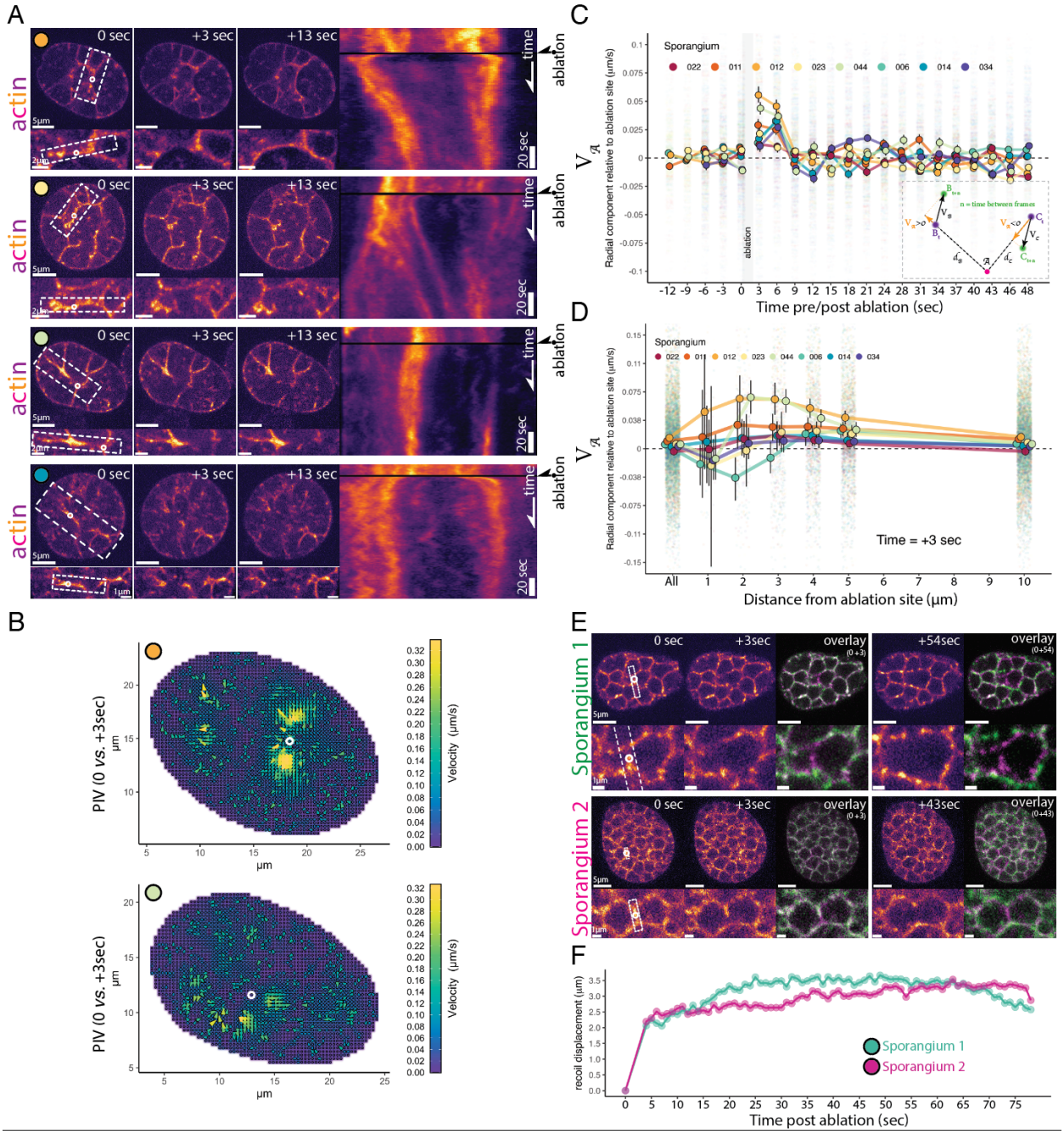

Figure 6. The actomyosin furrows of early cellularization and the edges of the late cellularization polyhedra are under tension. (A) Laser ablation of the actin furrows during early cellularization results in recoil. Four examples of sporangia ablation are shown. Colored circles correspond with sporangia shown in later panels. Each row shows still images of the sporangia just before laser ablation (0 sec, at white circle) and then 3 and 13 seconds after laser ablation, with dashed region inset below. The rectangle in each inset shows the 20-pixel wide selection used for the sum of intensity kymograph on the right. In each kymograph, the fast recoil response after the dark rows (ablation) is followed by contraction of the actin structure as if "repairing" the damaged region. **(B)** We used particle image velocimetry (PIV) to quantify the changes in the speed and direction of all actin structures of cellularization. Two examples (sporangia with corresponding color circles in panel A) of PIV velocity field plots

comparing the frames before laser ablation (0 sec) and after ablation (3 sec). Note vectors with high velocity (warm color) moving away—recoiling—from the ablation sites (white circles). **(C)** Laser ablation causes a high velocity recoil away from ablation site in all actin structures within 4μm of the ablation site. We use the radial component of the velocity ($V_{\mathcal{A}}$) relative to the ablation site ($\mathcal{A}$) to show movement only in the direction of the ablation site (away—postive—or towards—negative; see cartoon in inset). The short period of negative $V_{\mathcal{A}}$ that follows the recoil in most sporangia is consistent with the "repairing" contraction towards the ablation site. Color dots show mean values (corresponding sporangia shown with the same color circles of A) and error bars show 99% confidence interval of the mean by bootstrap. For visualization purposes we display data points within a range of -0.1 to 0.1 μm/s (this is 176417 points; 95% of the total data). **(D)** Radial component of the actin velocities ($V_{\mathcal{A}}$) relative to the ablation site (A) for vectors at different distances from the ablation site (*d* in cartoon) at three seconds after the start of ablation. For visualization purposes we display data points within a range of -0.15 to 0.15 μm/s (this is 23198 points; 97% of the total data). Note that highest velocities occur between 2-4μm from the ablation site in most sporangia (see supplementary figures 4-6). **(E)** Laser ablation of the cleavage furrows during late cellularization also results in recoil and dilation of the polyhedral geometry. Overlay for frames before and the first frame after the end of ablation (3 sec from the "before" image) and between the frame before and the frame showing near maximal recoil displacement (54 sec & 43 sec). **(F)** Recoil displacement caused by ablation of the sporangia (pink and green) shown in E, along the direction indicated by the white dotted rectangle in the inset. The recoil of the polyhedral edges shows a sharp fast recoil of about ~2μm—primarily from recoil of the cleavage furrow—followed by dilation of the surrounding polyhedra.

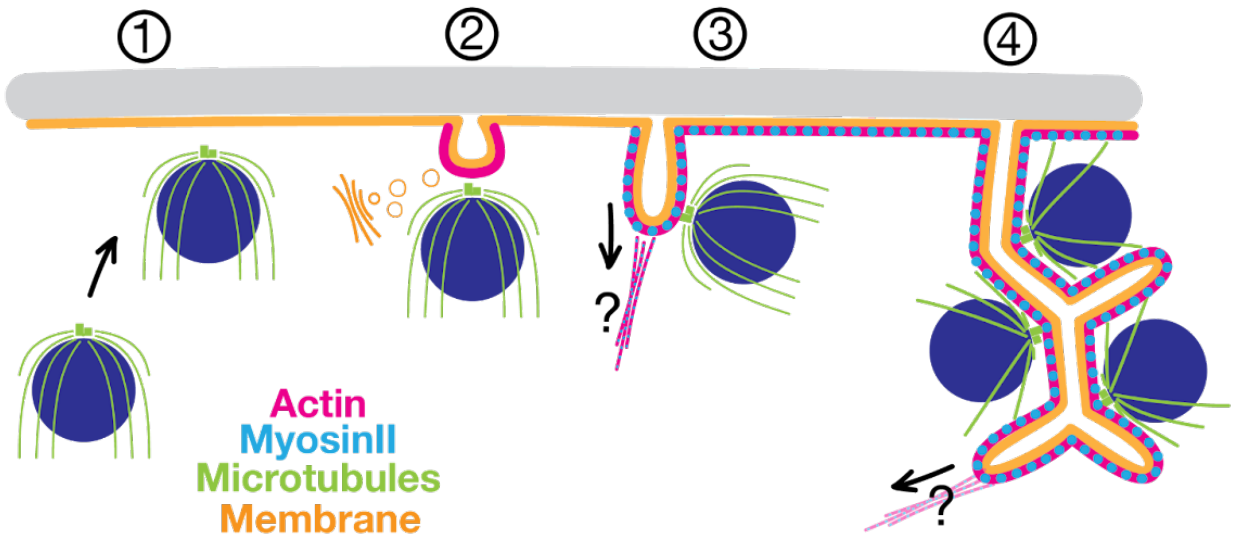

Figure 7. The model of chytrid 3D cellularization. (1) Nuclear cortical migration: Entry into cellularization is marked by the recruitment of nuclei to the plasma membrane, each nucleus with the centriolar centrosome facing toward the plasma membrane. **(2) Vesicular furrow initiation:** a vesicular membrane furrow initial is formed between the nuclear centriole and the plasma membrane. This stage does not depend on myosin-II and the membrane sourced from this stage onwards is derived from the Golgi apparatus. **(3) Furrow ingression and nuclear docking:** Actin and myosin-II drive together the extension of these vesicular furrows into tubular furrows that invade the cytoplasm. The nuclei remain attached to their furrows by the centrosomal region and are dragged inwards into the cytoplasm. Although nuclear docking may happen during furrow initiation (stage 2), we can only see it indirectly thus far due to their physical tethering during furrow ingression. **(4) Assembly of the polyhedral tessellation:** Tubular furrows branch and merge to generate the polyhedral territories of cellularization, each with a single nucleus inside. The microtubules play a role in proper nuclear distancing and geometry of the polyhedral territories. The ciliary axonemes extend in between the leaves of the double-membrane of the polyhedral faces. After a maturation time of the polyhedral tessellation, the zoospores undergo cell separation and swim or crawl out through an opening the the cell wall of the mother.

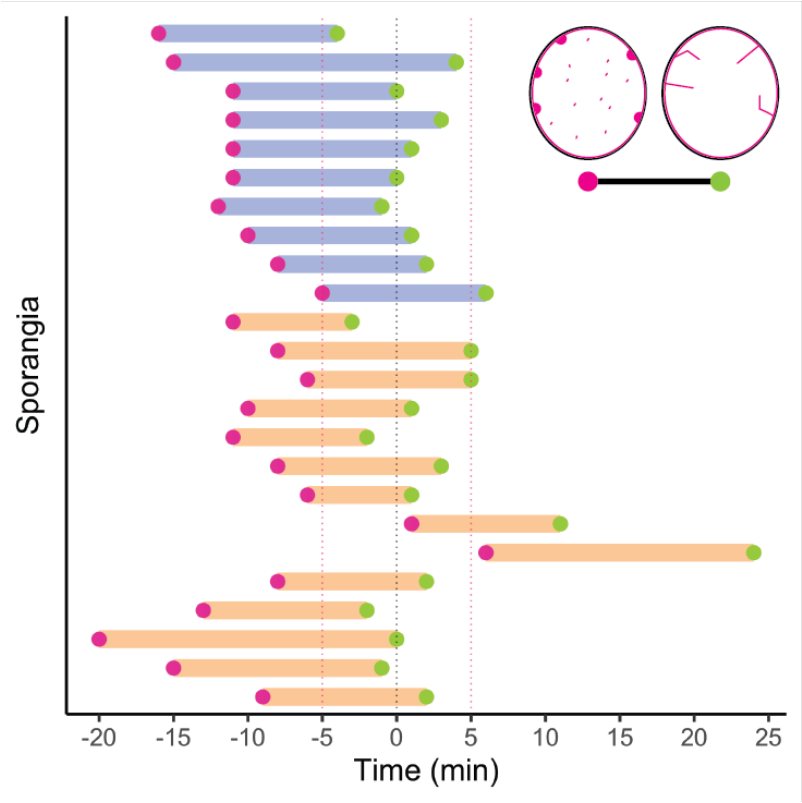

Figure S1. Furrow ingression coincides with peak cortical nuclear migration . Each sporangium (row) shows peak cortical nuclear ratio (CNR) at time 0 min. The color bar represent time relative to peak CNR from formation of the first vesicular furrow initial (magenta dot) to the moment the first furrow invades the cytoplasm (green dot). Note how most green dots are within 10 min around peak CNR. Different bar colors represent experiments from different days.

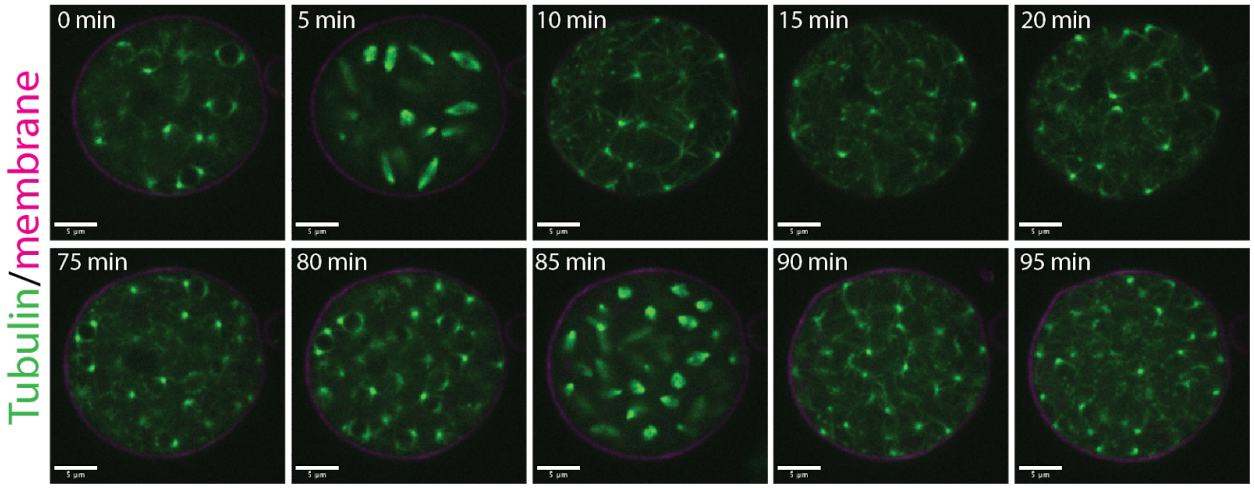

Figure S2. Nuclear-associated foci of fluorescently-tagged tubulin are likely chytrid centrosomes. Expression of fluorescently-tagged chytrid alpha-tubulin highlights centrosome-like foci at the poles of each nuclei that turn into opposing spindle poles during nuclear division. Scale bar is 5 microns.

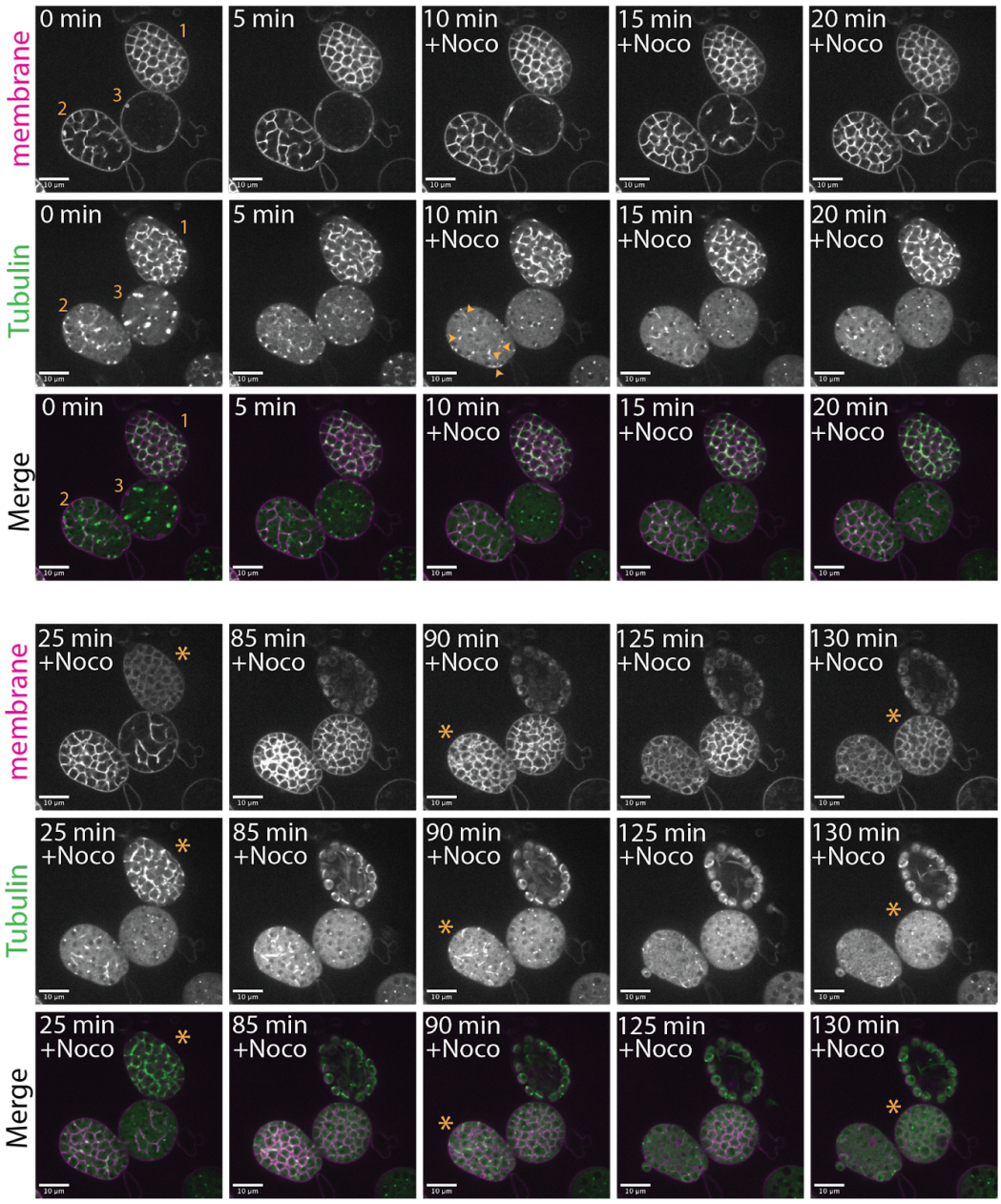

Figure S3. Cellularization in the presence of Nocodazole does not inhibit cellularization but produces defects in patterning and aciliated daughters. Example of three mother cells at different stages in cellularization during treatment with Nocodazole (10 min onwards). Note how Nocodazole causes disipation of fluorescent structures except for the bright foci at each nuclei (putative centrosome) and defects in polyhedral patterning. Mother 1 (see yellow numbers) is fully cellularized with daughters fully ciliated. This mother completes cellularization (25 min; asterisk) and daughters escape the mother's cell wall. Mother 2 is at stage 2 of cellularization (branching & merging) and shows some nuclei starting to extend their axoneme (yellow arrows; 10 min) by the time of treatment. This results in a combination of daughters with and without cilia, but still completes cellularization (90 min; asterisk). Mother 3 is at stage 1-2 of cellularization (furrow initiation). Cellularization is completed at 130 min (asterisk) and produces daughter that completely lack cilium. Scale bar 5 microns.

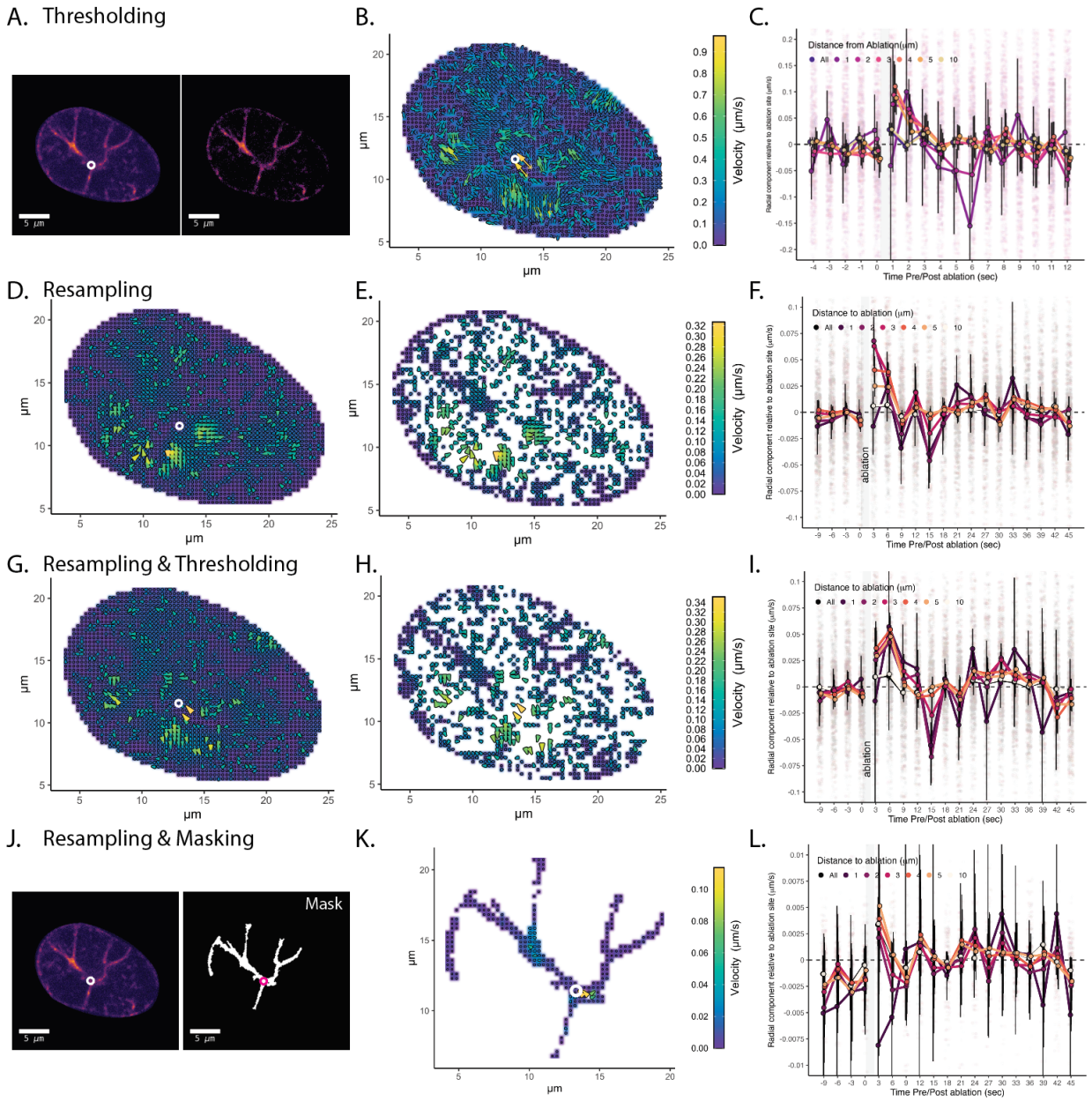

Figure S4. The signal of recoil after ablation from PIV analysis is robust to different ways of filtering and thresholding the data. (A). Example images before and after thresholding with Multi-Otsu. **(B)** Flow plot with local velocities estimated by PIV comparing the frame just before ablation (time 0) and the first frame after laser ablation (1 second from the end of ablation)—real time between images is 3 seconds, but time after the end of ablation is about 1 second. **(C)** Plot showing the radial component of velocities relative to the ablation site of all vectors vectors with magnitude above zero and that pass signal to noise test ('peak2peak'; threshold=0.5) from OpenPIV. Dots are mean values and error bars show 99% confidence interval of the mean by bootstrap. For visualization purposes only data within -0.2 and 0.2 µm/s is shown (42573 points; 85.6% of data). **(D)** Flow plot with local velocities estimated by PIV after resampling the image data every 3 seconds such that the complete time series reflect the same sampling rate as before-after laser ablation. **(E)**. Vectors from PIV that pass OpenPIV signal to noise test ('peak2peak'; threshold=0.5) and have a magnitude greater than zero are

the ones used for estimating the radial component of velocities relative to the ablation site. **(F)** Plot showing the radial component of velocities relative to the ablation site for the resampled images. Dots are mean values and error bars show 99% confidence interval of the mean by bootstrap. For visualization purposes only data within -0.2 and 0.2 μm/s is shown (537754 points; 95% of data). **(G)** Flow plot with local velocities estimated by PIV after a combination of resampling and thresholding. **(H)** Vectors from (G) that pass signal to noise and have magnitudes greater than zero. **(I)** Plot showing the radial component of velocities relative to the ablation site for the resampled and thresholded images. Dots are mean values and error bars show 99% confidence interval of the mean by bootstrap. For visualization purposes only data within -0.2 and 0.2 μm/s is shown (49370 points; 92% of data). **(J)** Masking the resampled images to limit the PIV analyses to the furrow regions (based on thresholding of the sum of the images before ablation). **(K)** Flow plot with local velocities estimated by PIV comparing the frame just before ablation (time 0) and the first frame after laser ablation (3 seconds). **(L)** Plot showing the radial component of velocities relative to the ablation site for the resampled and masked images. Dots are mean values and error bars show 99% confidence interval of the mean by bootstrap. For visualization purposes only data within -0.01 and 0.01 μm/s is shown (12042 points; 92% of data).

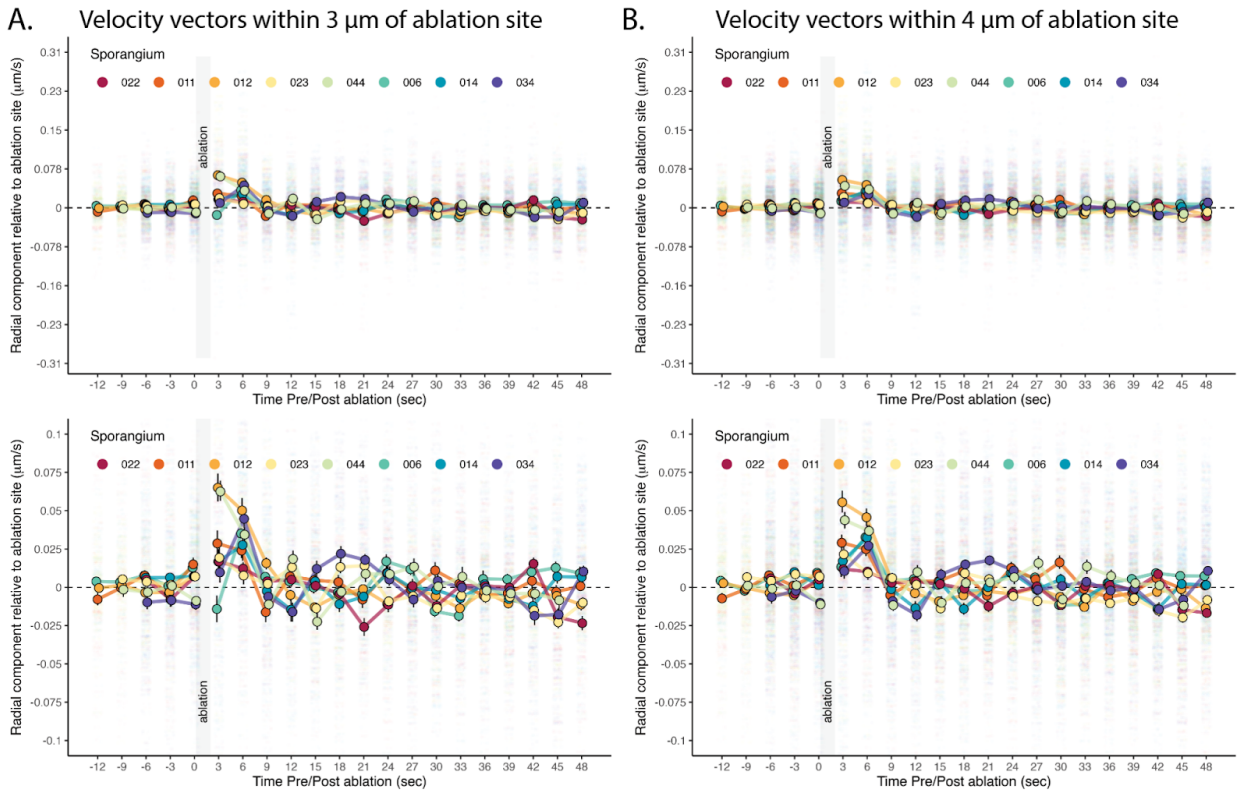

Figure S5. PIV retrieved high velocities within 3µm and 4µm from the ablation site when using data resampled every 3 seconds. (A). Plot showing the radial component relative to the ablation site (velocities away from—positive—or towards—negative—the ablation site) within 3µm from the ablation site. Bottom shows an enlarged version of top figure. For visualization purposes we display data points within a range of -0.1 to 0.1 µm/s (this is 111009 points; 95% of the total data). **(B)** Plot showing the radial component relative to the ablation site (velocities away from—positive—or towards—negative—the ablation site) within 4 µm from the ablation site. This is the data shown in Figure 6 in the main text. Bottom panel shows enlarged version of top plot (Figure 6 data). Dots are mean values and error bars show 99% confidence interval of the mean by bootstrap. For visualization purposes we display data points within a range of -0.1 to 0.1 µm/s (this is 176417 points; 95% of the total data).

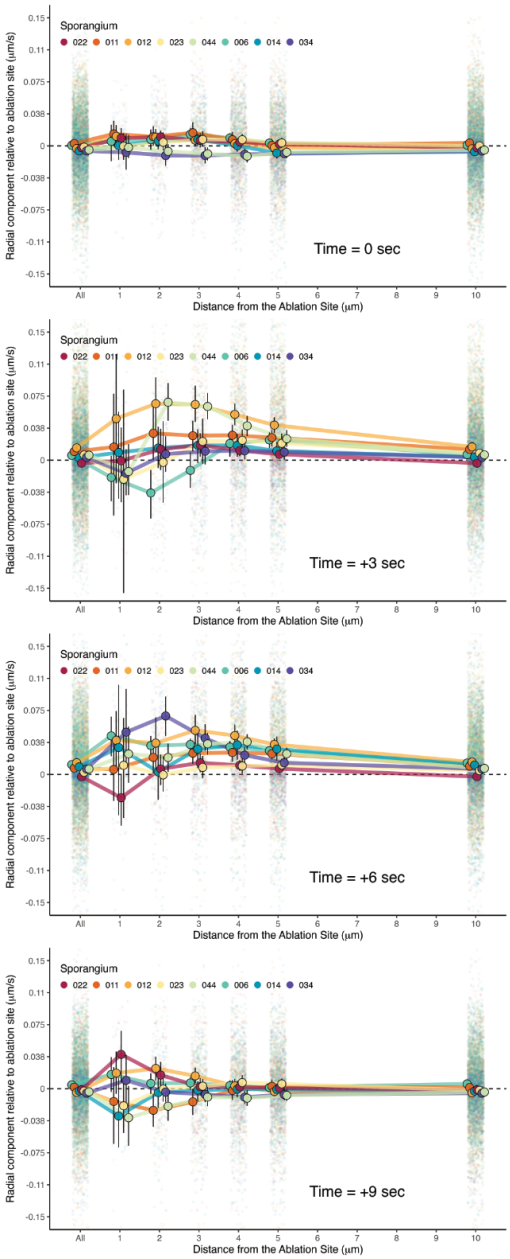

Figure S6. Velocities away from or towards the ablation site at increasing distances from the ablation site during 3, 6, and 9 seconds after the beginning of ablation. Top. Plot showing the radial component relative to the ablation site (velocities away from—positive—or towards—negative—the ablation site) just before ablation. “All” uses all velocities within the sporangium that pass signal to noise OpenPIV test and have a magnitude greater than zero. The other plots show distribution of velocities 3,6, and 9 seconds after ablation. Note that the greatest recoil velocities are detected between 2-4 microns from the ablation site and 3 seconds after ablation (4 seconds for sporangium 034 & 014). Dots are mean values and error bars show 99% confidence interval of the mean by bootstrap. For visualization purposes 25256 points (99%), 23198 points (97%), 24239 points (98%), and 24628 points (99%) are shown for each plot respectively.

SUPPLEMENTARY VIDEO LEGENDS

Supplementary Video 1. F-actin colocalizes with the cellularization membrane polyehedra of a live chytrid mother cell about to reach peak cellularization. F-actin (Lifeact-mClover3) shown in green and membrane (FM4-64) in magenta. Note a small section is not completely cellularized. Laser-scanning confocal imaging. Mother cell is about 20 microns deep: Z-plane sweep of 138 Z-stacks, each 0.148 microns. Scale 5 microns.

Supplementary Video 2. Distribution of nuclei during chytrid peak cellularization. Nuclei (RbNLS-mClover3) shown in green and membrane (FM4-64) in magenta. Laser-scanning confocal imaging. Mother cell is about 20 microns deep: Z-plane sweep of 130 Z-stacks, each 0.148 microns. Scale 5 microns.

Supplementary Video 3. Distribution of myosin-II light regulatory chain (MLRC) during chytrid peak cellularization. A probe of myosin-II activity, MLRC (MLRC-mClover3) in shown in green and membrane (FM4-64) in magenta. Laser-scanning confocal imaging. Mother cell is about 20 microns deep: Z-plane sweep of 136 Z-stacks, each 0.148 microns. Scale 5 microns.

Supplementary Video 4. Microtubule architecture during chytrid peak cellularization. Chytrid alpha-tubulin (mClover3-alpha-Tubulin) in shown in green and membrane (FM4-64) in magenta. Laser-scanning confocal imaging. Z-plane sweep of 28 Z-stacks, each 0.6 microns. Scale 5 microns.

Supplementary Video 5. Nuclear dynamics during chytrid cellularization. Nuclei visualized with fluorescently-tagged histone H2B (H2B-tdTomato) are shown in green and membrane (FM4-64) in magenta. Spinning-disk confocal time-lapse. Sampling rate of one image per minute. You can see the last two nuclear divisions before the chytrid mother enters cellularization. Scale 5 microns.

Supplementary Video 6. Example of Nuclear cortical migration during chytrid cellularization. Nuclei visualized with fluorescently-tagged histone H2B (H2B-tdTomato) are shown in green and membrane (FM4-64) in magenta. Nuclei reach peak cortical ratio around 295 minutes. Spinning-disk confocal time-lapse. Sampling rate of one image per minute. You can see the last two nuclear divisions before the chytrid mother enters cellularization. Scale 5 microns.

Supplementary Video 7. Example 1 of outward-facing nuclear centrosomes during entry into cellularization. Fluorescently-tagged tubulin (mClover3-alpha-Tubulin) shown in green and membrane (FM4-64) in magenta. Note how during cortical nuclear recruitment, the nuclear-associated centrosomes are often positioned towards the plasma membrane (100-110 min). Spinning-disk confocal time-lapse. Sampling rate of one image every five minutes. Scale 5 microns.

Supplementary Video 8. Example 2 of outward-facing nuclear centrosomes during entry into cellularization. Fluorescently-tagged tubulin (mClover3-alpha-Tubulin) shown in green and membrane (FM4-64) in magenta. Mitotic spindles are visible during nuclear division (85min), and during entry into cellularization (140 min). Note how during cortical nuclear recruitment, the nuclear-associated centrosomes are often positioned towards the plasma membrane (135 min). Nuclei remain tethered to the invading furrow via the centrosome. Spinning-disk confocal time-lapse. Sampling rate of one image every five minutes. Scale 5

1300 microns.
1301
1302 **Supplementary Video 9. Example 3 of outward-facing nuclear centrosomes during entry**
1303 **into cellularization.** Fluorescently-tagged tubulin (mClover3-alpha-Tubulin) shown in green
1304 and membrane (FM4-64) in magenta. Note how during cortical nuclear recruitment, the
1305 nuclear-associated centrosomes are often positioned towards the plasma membrane (25 min).
1306 Nuclei remain tethered to the invading furrow via the centrosome. Spinning-disk confocal
1307 time-lapse. Spinning-disk confocal time-lapse. Sampling rate of one image every five minutes.
1308 Scale 5 microns.
1309
1310 **Supplementary Video 10. Example 4 of microtubular dynamics during chytrid**
1311 **cellularization.** Fluorescently-tagged tubulin (mClover3-alpha-Tubulin) shown in green and
1312 membrane (FM4-64) in magenta. Spinning-disk confocal time-lapse. Spinning-disk confocal
1313 time-lapse. Sampling rate of one image every five minutes. Scale 5 microns.
1314
1315 **Supplementary Video 11. Chytrid centrioles appear to dock and tether to the**
1316 **cellularization furrows during chytrid cellularization (Example 1).** Fluorescently-tagged
1317 component of the centriole SAS6 (SAS6-mClover3) shown in green and membrane (FM4-64)
1318 in magenta. Spinning-disk confocal time-lapse. Spinning-disk confocal time-lapse. Sampling
1319 rate of one image every three minutes. Scale 5 microns.
1320
1321 **Supplementary Video 12. Chytrid centrioles appear to dock and tether to the**
1322 **cellularization furrows during chytrid cellularization (Example 2).** Fluorescently-tagged
1323 component of the centriole SAS6 (SAS6-mClover3) shown in green and membrane (FM4-64)
1324 in magenta. Spinning-disk confocal time-lapse. Spinning-disk confocal time-lapse. Sampling
1325 rate of one image every three minutes. Scale 5 microns.
1326
1327 **Supplementary Video 13. Chytrid mothers exposed to Brefeldin-A during late**
1328 **cellularization show collapse of the cellularization furrows.** Fluorescently-tagged tubulin
1329 (mClover3-alpha-Tubulin) shown in green and membrane (FM4-64) in magenta. Spinning-disk
1330 confocal time-lapse. Sampling rate of one image every three minutes. Scale 5 microns.
1331
1332 **Supplementary Video 14. Chytrid mothers exposed to Brefeldin-A before entry into**
1333 **cellularization fail to enter cellularization.** Fluorescently-tagged tubulin
1334 (mClover3-alpha-Tubulin) shown in green and membrane (FM4-64) in magenta. Spinning-disk
1335 confocal time-lapse. Sampling rate of one image every three minutes. Scale 5 microns.
1336
1337 **Supplementary Video 15. The actin-based furrows of early cellularization are under**
1338 **tension and recoil where severed by laser ablation (Example 1).** Spinning-disk confocal
1339 time-lapse imaging of central plane of a strain expressing the F-actin probe Lifeact-mClover.
1340 The actin structures are severed using a laser. Note the fast recoil response after ablation.
1341 Scale 5 microns.
1342
1343 **Supplementary Video 16. The actin-based furrows of early cellularization are under**
1344 **tension and recoil where severed by laser ablation (Example 2).** Spinning-disk confocal
1345 time-lapse imaging of central plane of a strain expressing the F-actin probe Lifeact-mClover.
1346 The actin structures are severed using a laser. Note the fast recoil response after ablation.
1347 Scale 5 microns.
1348
1349 **Supplementary Video 17. The actin-based furrows of early cellularization are under**
1350 **tension and recoil where severed by laser ablation (Example 3).** Spinning-disk confocal

time-lapse imaging of central plane of a strain expressing the F-actin probe Lifeact-mClover. The actin structures are severed using a laser. Note the fast recoil response after ablation. Scale 5 microns.

Supplementary Video 18. The actin-based furrows of early cellularization are under tension and recoil where severed by laser ablation (Example 4). Spinning-disk confocal time-lapse imaging of central plane of a strain expressing the F-actin probe Lifeact-mClover. The actin structures are severed using a laser. Note the fast recoil response after ablation. Scale 5 microns.

Supplementary Video 19. The actin-based furrows of early cellularization are under tension and recoil where severed by laser ablation (Example 6). Spinning-disk confocal time-lapse imaging of central plane of a strain expressing the F-actin probe Lifeact-mClover. The actin structures are severed using a laser. Note the fast recoil response after ablation. Scale 5 microns.

Supplementary Video 20. The actin-based furrows of early cellularization are under tension and recoil where severed by laser ablation (Example 7). Spinning-disk confocal time-lapse imaging of central plane of a strain expressing the F-actin probe Lifeact-mClover. The actin structures are severed using a laser. Note the fast recoil response after ablation. Scale 5 microns.

Supplementary Video 21. The polyhedra of chytrid cellularization are under tension (Example 1). Spinning-disk confocal time-lapse imaging of central plane of a strain expressing the F-actin probe Lifeact-mClover. The actin structures are severed using a laser. Note the fast recoil response after ablation followed by deformation of the neighboring polyhedra. Scale 5 microns.

Supplementary Video 22. The polyhedra of chytrid cellularization are under tension (Example 2). Spinning-disk confocal time-lapse imaging of central plane of a strain expressing the F-actin probe Lifeact-mClover. The actin structures are severed using a laser. Note the fast recoil response after ablation followed by deformation of the neighboring polyhedra. Scale 5 microns.